

## Multiscale Analysis of Nanoindentation-Induced Defect Structures in Gum Metal

R. P. Sankaran<sup>a,\*</sup>, V. B. Ozdol<sup>b</sup>, C. Ophus<sup>b</sup>, J. Kacher<sup>b</sup>, C. Gammer<sup>c</sup>, S. Govindjee<sup>d</sup>, A. M. Minor<sup>a,b</sup> and J. W. Morris, Jr.<sup>a</sup>

<sup>a</sup>Department of Materials Science and Engineering, <sup>d</sup>Department of Civil and Environmental Engineering, University of California, Berkeley, CA 94720

<sup>b</sup>National Center for Electron Microscopy, Molecular Foundry, Lawrence Berkeley National Laboratory, Berkeley, CA 94720

<sup>c</sup>Erich Schmid Institute of Materials Science, Austrian Academy of Sciences, Leoben, Austria

### Abstract

Using *ex-situ* transmission electron microscopy and the recently developed nanoprobe diffraction (NPD) technique, we characterize a nanoindented solution treated gum metal. Lattice rotations are resolved at a 1.2 nanometer length-scale and shown to be continuous within the nanoindentation pit; further, it is shown that these can be accommodated by a reasonable number of geometrically necessary dislocations at a density of  $\sim 10^{15}/\text{m}^2$ . We additionally provide direct evidence that dislocations within the nanoindent, rather than secondary phase nanoparticles, can serve as potent barriers to dislocation motion. We also demonstrate that plasticity in these alloys under nanoindentation can be accommodated solely by dislocation nucleation and propagation, with no competing deformation mechanisms present. Conventional transmission electron microscopy and “ $\mathbf{g}\cdot\mathbf{b}$ ” analysis reveal the presence of dislocations on  $\langle -111 \rangle \{110\}$  slip systems and highly localized plastic deformation in the form of shear bands on  $\langle 111 \rangle \{-1-12\}$  slip systems, similar to previously observed “giant faults”.

### Keyword

gum metals; metastable beta-titanium alloys; nanoindentation; nanoprobe diffraction (NPD, or nanobeam electron diffraction, NBED); strain mapping

## 1. Introduction

Beta ( $\beta$ ) (BCC) Ti-Nb alloys are attractive for bioimplants because of their low elastic moduli, biocompatibility, superelasticity, and shape-memory behavior [1,2,3]. A subset of these alloys termed “gum metals”, developed by Toyota R&D [4], possess a low shear modulus in the  $\langle 111 \rangle_{\beta}$  direction and high yield strength. They also exhibit unusual mechanical behavior and defect structures, especially when tested after severe cold working. In the original investigations, their shear strength seemed to approach the ideal value at elastic instability ( $0.11G_{\langle 111 \rangle}$ ) [5], given the calculated elastic constants available at the time [6, 7]. The purported deformation structures supported the notion of ideal shear operating via giant fault formation and atomic-scale “nanodisturbances” [4,8,9].

Further research on this interesting material has revealed the complexity of its behavior in both the cold-worked and solution-treated conditions. Its possible deformation modes have been shown to include not only “giant faults”, but ordinary dislocation flow [10, 11, 12, 13], deformation twinning [14, 15, 16], and transformation-induced plasticity via several different product phases [14,15,16], including possible transient phases that grow and shrink with the applied load [10, 16, 17]. As work on single-crystal variants has shown, both the mechanical response and the dominant deformation mechanism change with the sign and orientation of the applied stress [18, 19]. Both the phases that are present and the deformation behavior are also sensitive to minor changes in composition, as is typical of beta-Ti alloys. Given that this alloy was intentionally designed to reside at the limit of stability of the BCC phase, this complex behavior is not surprising, but it does emphasize the need for careful experimentation and characterization if the various aspects of its behavior are to be well understood.

1  
2  
3  
4 One mechanical test that has proven useful in clarifying the fundamentals of mechanical  
5 behavior in recent years is nanoindentation, particularly when coupled with high-resolution  
6 characterization studies. A nanoindenter tests material that is ordinarily defect-free and imposes  
7 its maximum stress slightly beneath the contacted surface so that surface effects should not  
8 dominate the initiation of deformation [20]; there is strong evidence that nanoindentation can  
9 produce deformation at or very close to ideal strength [21], allowing the deformation modes that  
10 are activated to be studied in detail.  
11  
12  
13  
14  
15  
16  
17  
18  
19  
20

21 Prior work in this laboratory specifically included nanoindentation experiments on gum  
22 metal (solution-treated), coupled with high-resolution TEM studies of the deformation near the  
23 indentation pits [22]. Those studies produced a number of useful observations, but also  
24 identified three puzzling features of the deformation pattern that needed to be clarified. First,  
25 while a dense distribution of mobile dislocations was identified in the periphery of the pits, the  
26 centers of the pits appeared to be featureless, with no dislocations resolved. This suggests that  
27 some other mechanism might be operative. Second, the material within these featureless regions  
28 exhibited apparently continuous lattice rotations as the center of the pit was approached. Since  
29 local lattice rotations are ordinarily stabilized by crystal defects, this observation raised a serious  
30 question of what these defects might be. Third, the dislocations in the periphery of the pits were  
31 severely bowed, showing themselves to be strongly pinned by local obstacles. The nature of  
32 these obstacles could not be determined, raising the question of whether they are inherent  
33 features of the alloy, such as nano-precipitates, that might play an important role in its  
34 strengthening.  
35  
36  
37  
38  
39  
40  
41  
42  
43  
44  
45  
46  
47  
48  
49  
50  
51  
52  
53

54 The present study aims to understand the observed behavior using *ex-situ* transmission  
55 electron microscopy (TEM) of solution treated gum metal (STGM) after nanoindentation.  
56  
57  
58  
59  
60  
61  
62  
63  
64  
65

1  
2  
3  
4 Cross-sections of nanoindented STGM are analyzed via conventional TEM and annular dark  
5 field (ADF) imaging to give a more complete picture of the dislocation structure beneath the  
6 indent. Nanoprobe diffraction (NPD) is used to determine the exact nature of the sustained  
7 rotations and strain near the indent pit and to determine whether any secondary phases are  
8 mechanically induced. As we shall show, these more probative characterization techniques  
9 reveal a complex distribution of previously undetected dislocations that can fully account for the  
10 deformation field of the indentation pit. To our knowledge, ours is the first fundamental and  
11 detailed study of its kind to comprehensively analyze the defect structures that occur in a BCC  
12 material under nanoindentation, and the results and observations could potentially be more  
13 broadly applicable to BCC metals.  
14  
15  
16  
17  
18  
19  
20  
21  
22  
23  
24  
25  
26  
27  
28

## 29 **2. Materials and Methods**

### 30 2.1. Sample preparation procedure

31  
32 Material used in this investigation was supplied by Toyota Central R&D Laboratories,  
33 Nagakute, Japan as round bars of STGM with a nominal composition of 73.1Ti-23Nb-0.7Ta-  
34 2Zr-1.2O at.% These were fabricated by cold-isostatic pressing of elemental powders, sintering  
35 at 1300°C, hot forging at 1150°C, and solution-treating in Ar at 900°C [4]. Severe cold work of  
36 90% was imparted by rotary swaging at room temperature (CWGM) followed by solution-  
37 treating in air for 30 minutes at 900°C (STGM). The STGM bars were cut perpendicular to the  
38 swaging direction into discs ~300 μm thick, disc cut to 3mm diameter, mechanically polished to  
39 ~100 μm thickness with SiC paper and jet polished on one surface in a Fischione Model 1010  
40 twin-jet using an electrolyte solution of 4 vol% perchloric acid, 25 vol% butanol, and 71 vol%  
41 methanol at -30°C and 42V for 2min. Electropolishing provides a smoother, damage-free surface  
42 than mechanical polishing can, enabling acquisition of more reliable nanoindentation data. As  
43  
44  
45  
46  
47  
48  
49  
50  
51  
52  
53  
54  
55  
56  
57  
58  
59  
60  
61  
62  
63  
64  
65

1  
2  
3  
4 jet polishing results in a slight dimpling of the sample, only one side of the specimen was  
5  
6 polished. The other side, covered with non-adhesive Teflon<sup>®</sup> tape to prevent polishing, retained  
7  
8 a completely flat base for mounting on the nanoindentation stage. The electropolished side  
9  
10 underwent nanoindentation *ex-situ* in a Hysitron Triboindenter<sup>®</sup> fitted with a diamond Berkovich  
11  
12 tip. A triangular load-control function with 25mN maximum load and a loading/unloading rate  
13  
14 of 5mN/s was used. The resulting load-displacement curves are similar to those in [22], in which  
15  
16 no “pop-in” events are observed. Figure 1(top), schematically shows the sample set-up, where  
17  
18 the indentation axis is nominally parallel to the swaging axis  $\langle 110 \rangle_{\beta}$ .  
19  
20  
21  
22

23  
24 The cross-section of one of the indents was prepared for TEM observation through the “*in-*  
25  
26 *situ* lift-out technique” [23] using an FEI Strata dual beam SEM/FIB with Ga<sup>+</sup> ion source  
27  
28 equipped with an Omniprobe micromanipulator. The indent was first coated with a 2 $\mu$ m thick  
29  
30 protective film of Pt and thinned to an initial thickness of 200nm at 30kV. An SEM image of the  
31  
32 thinned lamella prior to lift-out is given in Figure 1(bottom). After the lamella was attached to  
33  
34 the TEM grid, it was further milled and cleaned to a thickness of ~100nm at 6kV and 300pA.  
35  
36  
37

## 38 2.2. Experimental facilities and parameters

39  
40  
41 Conventional TEM was performed on a JEOL 3010 microscope at 300 kV. ADF-STEM  
42  
43 imaging was performed on an FEI Titan with a CEOS probe aberration corrector at 300 kV with  
44  
45 0.5Å probe size and 17.2mrad convergence semi-angle. ADF signal was collected at an inner  
46  
47 collection semi-angle range of 24-35mrad. Scanning Nanoprobe Diffraction (NPD) was  
48  
49 performed on an FEI Titan operating at 300kV in STEM mode. During High-Angular Dark  
50  
51 Field HAADF imaging, a diffraction pattern was acquired for every probe position. The three  
52  
53 independent condenser lenses enable STEM imaging with various convergence semi-angles. A  
54  
55 sub-nm electron probe with a convergence semi-angle of ~0.9-1 mrad was used in nanoprobe  
56  
57  
58  
59  
60  
61  
62  
63  
64  
65

1  
2  
3  
4 mode, yielding diffraction patterns with non-overlapping spots while enabling good spatial  
5  
6 resolution (<1nm). Full diffraction patterns with 1024x1024 pixels resolution were captured  
7  
8 relatively rapidly (0.1s) with the Gatan Orius 830 diffraction camera and custom software  
9  
10 implemented in DigitalMicrograph.  
11  
12

### 13 14 2.3. Nanoprobe diffraction analysis algorithm

15  
16 Diffraction patterns were analyzed offline using custom MATLAB code. Peak positions  
17  
18 were located using a cross-correlation routine. High-pass filtering was performed prior to this  
19  
20 step to remove the internal structure of diffraction disks. A pure cross-correlation method with  
21  
22 filtering was optimal due to the thickness of the sample [24]. A peak-fitting algorithm was used  
23  
24 on the original diffraction pattern to refine the initial peak position determined from the cross-  
25  
26 correlation routine. Strain and rotation maps were then computed by calculating basis vectors  
27  
28 for each pattern via a least squares approach. The deformation gradient tensor,  $\mathbf{A}$ , was computed  
29  
30 with respect to a reference lattice, which was determined by calculating the median basis vectors  
31  
32 from all the diffraction patterns included in the bottom half of the data set presented in Figure 6a.  
33  
34 Thus, the color indices which we present are deviations of rotation and strain from this nominally  
35  
36 deformation-free part of the sample. The deformation gradient was decomposed into stretch and  
37  
38 rotation matrices via the singular value decomposition algorithm [25] such that  $\mathbf{A} = \mathbf{UH}$ , where  
39  
40  $\mathbf{U}$  and  $\mathbf{H}$  are rotation and stretch matrices, respectively. The rotation value,  $\theta$ , was computed  
41  
42 from the rotation matrix, since  $\mathbf{U} = \begin{bmatrix} \cos \theta & -\sin \theta \\ \sin \theta & \cos \theta \end{bmatrix}$ . We used the (Lagrangian) Biot strain  
43  
44 measure  $\mathbf{E} = \mathbf{H} - \mathbf{I}$ . If the strain matrix is computed this way directly from the change in  
45  
46 reciprocal lattice basis vectors, the strain components would represent the strains in reciprocal  
47  
48 space. Since the measured lattice basis vectors were determined from the diffraction patterns, the  
49  
50 real space strains were computed with  $\mathbf{E}_{real\ space} = \mathbf{I} - \mathbf{H}$ .  
51  
52  
53  
54  
55  
56  
57  
58  
59  
60  
61  
62  
63  
64  
65

### 3. Results

#### 3.1. Nanoindentation data and analysis of defect structures

The load displacement curves obtained from nanoindentation, shown in Figure 2, are similar to those presented in [22], in which no “pop-in” events are observed. Using procedure indicated in Oliver and Pharr [26], mean hardness is calculated as 2.63GPa with a standard deviation of 0.06GPa. This value is consistent with previous hardness measurement of 250Hv (~ 2.45GPa) for both STGMs and CWGMs obtained by Saito et al. [27].

Immediately from Figures 3a and b, we observe that the nanoindentation process produces a large number of dislocations along with other defect structures such as shear bands and small angle grain boundaries. The clearly distinguishable dislocations 1-5  $\mu\text{m}$  away from the pit appear as relatively long and discrete line defects, whereas the defects within the region immediately adjacent to the pit are not as easily observed or understood. This observation is at first consistent with the results of Withey et al. [22], particularly the supposed lack of dislocations observed in the indent pit. To understand the complex defect structure generated within the nanoindent, we perform (1) conventional “ $\mathbf{g}\cdot\mathbf{b}$ ” analysis on the discrete dislocations and shear bands further away from the indent pit, (2) ADF imaging to determine the origin of bowing and kinking observed in many of the dislocations and (3) NPD to quantify the large rotations and strains immediately adjacent to the indent pit.

##### 3.1.1. Dislocation analysis: Burgers and line vector determination

Gum metals, having a BCC crystal structure, are likely to have dislocations with Burgers vector,  $\mathbf{b}$ , of  $\langle 111 \rangle$ -type. TEM images taken under a two-beam condition with the  $\mathbf{g} = (200)$  reflection should render all dislocations of this type visible. Thus, in Figures 3c and 3d we present TEM images taken with both the  $\mathbf{g}=(200)$  and  $\mathbf{g}=(110)$  reflections, respectively, to

1  
2  
3  
4 observe a majority of the dislocations generated within the sample. Of the easily distinguishable  
5  
6 dislocations about the nanoindent, the discrete ones appear to be broadly divided into four  
7  
8 configurations. Example dislocations within these four groupings are outlined in Figure 3c and  
9  
10 d: the ones indicated in blue are referred to as horizontal, denoted by “H”; magenta as vertical,  
11  
12 “V”; red as “Slant Up” and “Slant Down”, “SU/SD”; and those within the yellow as Shear Band,  
13  
14 “SB”. The V- and H-type appear on both sides of the plastic zone, and the SU and SD types lie  
15  
16 near the middle. We performed extensive “ $\mathbf{g}\cdot\mathbf{b}$ ” analysis and a coarse line trace analysis to  
17  
18 determine the Burgers vectors and sense vectors of these dislocations groups. Details of this  
19  
20 analysis are given in Supplementary Materials for each configuration, and the results are  
21  
22 presented in Table 1. For the H and SU/SD groups, there is some ambiguity in determining the  
23  
24 exact slip system. But, taking the data overall, we find that the observed discrete dislocations  
25  
26 beneath the indent are consistent with slip systems typically found in BCC materials. Specifically,  
27  
28 the two groupings, H and SU/SD, are comprised of dislocations consistent with the  $\langle -111 \rangle \{110\}$   
29  
30 slip system; the V-type of screw dislocations with  $\mathbf{b}$  of  $\langle 111 \rangle$ -type; and the SB dislocations in  
31  
32 the shear bands reside on the  $\langle 111 \rangle \{-1-12\}$ -type slip system. There may be other clearly  
33  
34 distinguishable dislocations not belonging to these groups, but the majority of the dislocations  
35  
36 further from the pit reside on the slip systems stated. Lastly, the presence of such dislocation  
37  
38 configurations clearly demonstrates that the defect structure generated from nanoindentation has  
39  
40 a certain order and structure.  
41  
42  
43  
44  
45  
46  
47  
48  
49

### 50 3.1.2. ADF STEM imaging: dislocation-dislocation interactions

51 We next characterize the structures beneath the indent using lower magnification ADF and  
52  
53 atomic resolution STEM imaging to further elucidate the nature of pinning points found in this  
54  
55 study (Supplementary Materials) and previous studies [22, 12]. Due to enhanced diffraction and  
56  
57  
58  
59  
60  
61  
62  
63  
64  
65



1  
2  
3  
4 strain contrast, ADF imaging conditions greatly aid in visualizing dislocations, enabling a better  
5  
6 qualitative understanding of their true density and interactions.  
7  
8

9 ADF images of the regions underneath the nanoindent at various magnifications are  
10 presented in Figure 4, where we notice the dislocations appear white under dark field conditions.  
11  
12 The observed dislocation arrangement is consistent with our previous results obtained from  
13  
14 conventional TEM imaging. We notice again that a very large dislocation density is sustained  
15  
16 within the deformed region beneath the indent, and, from Figure 4a, we determine that while  
17  
18 there are no easily distinguishable defects immediately adjacent to the pit, we can clearly  
19  
20 recognize the previously observed dislocation groups (H, V, SU/SD, SB) further away from the  
21  
22 indent impression. Additional dislocations, not encompassed in these groups, are also present,  
23  
24 but are difficult to discern due to the large amount of dislocation entanglement clearly observed  
25  
26 in Figures 4b-d. Interestingly, within the bottom shear band in Figure 4d, we observe a  
27  
28 dislocation cell network (DCN) within the band has formed. In the one above it, the band  
29  
30 appears to be in an initial stage of DCN formation with heavily bowed dislocations with one  
31  
32 overlapping segment.  
33  
34  
35  
36  
37  
38  
39

40 To understand the cause of this severe dislocation bowing, we **focus** our attention on the  
41  
42 boundary of the plastic zone. It is in these regions, just at the border between the deformed and  
43  
44 the nominally un-deformed regions, that we find the dislocation density is significantly lower  
45  
46 allowing for a clearer view of any dislocation interactions. Specifically, the area imaged in  
47  
48 Figure 4c contains a region of lower dislocation density next to the indent impression. We  
49  
50 observe a particular dislocation situated ~150-200 nm away from the high-density zone which is  
51  
52 outlined in Figure 5a. A higher resolution ADF image of this dislocation is presented in Figure  
53  
54 5b, in which it appears heavily bowed with a defect structure/pinning point ahead of its cusp.  
55  
56  
57  
58  
59  
60  
61  
62  
63  
64  
65

1  
2  
3  
4 Increasing the resolution further, we present an atomic resolution image in Figure 5c. The  
5  
6 pinning point appears as a linear defect with a complex atomic motif, in which extra atomic  
7  
8 columns appear between the BCC column locations (where the BCC-Ti matrix is oriented  
9  
10 nominally along [001] zone axis.) A model of the superlattice motif (green) is superimposed on  
11  
12 the BCC matrix (red) in Figure 5d. In the model, it is apparent the superlattice is best described  
13  
14 as helicoidal atomic displacements about the core of a mixed dislocation [28, 29]. Here, the  
15  
16 mixed dislocation is ~20 atomic columns wide (~4.5nm) with an observed length of ~7nm. The  
17  
18 Burgers vector, **b**, of the dislocation appears to lie along the [110] direction. As the ADF image  
19  
20 is a projection down the nominal [001] zone axis, the [-1-11] and [-1-1-1] directions in projection  
21  
22 coincide with the [110] direction. Thus, we determine **b** of the dislocation to be consistent with  
23  
24  $a/2\langle 111 \rangle$ -type, supporting the result from the “**g•b**” analysis in Section 3.1.1. The sense of the  
25  
26 dislocation, **u**, appears to lie along the projected [00-2] direction, but cannot be exactly  
27  
28 determined from one image. We conclude the bowing of the original dislocation is due to elastic  
29  
30 interaction with this mixed dislocation.  
31  
32  
33  
34  
35  
36  
37

### 38 3.1.3. Nanoprobe diffraction (NPD): continuous lattice rotations in STGM

39  
40 To complete our analysis, we examine regions closer to the indent, where higher stresses are  
41  
42 endured. As previously mentioned, ADF and conventional TEM imaging indicate that the  
43  
44 dislocations adjacent to the indent pit are too dense to be easily observed singularly or discretely  
45  
46 (Figure 4a, Figure 3a and 3b). Withey et al. [22] provided some evidence indicating that STGMs  
47  
48 exhibit a continuous rotation about specific axes within the nanoindentation pit. To better  
49  
50 understand the deformation behaviors and quantify the observed lattice rotations, we provide  
51  
52 rotation and strain maps calculated from the NPD data in Figures 6-8 measured from different  
53  
54 regions of the nanoindent. The foil normal is very close to the [001] zone, and we tilted to this  
55  
56  
57  
58  
59  
60  
61  
62  
63  
64  
65

1  
2  
3  
4 axis for acquiring all diffraction patterns. The x and y directions for the strain component  
5  
6 calculation are defined to be in the [-1-10] and [1-10] directions, respectively, of the reference  
7  
8 lattice (consistent with the indexing of the diffraction pattern in Supplementary Fig. 3). We note  
9  
10 here that the resultant rotation and strain maps obtained from the NPD technique given in  
11  
12 Figures 6-8 show outliers, noisy edges, and, in some cases, horizontal “streaking”. Horizontal  
13  
14 streaks are due to the Titan PC pausing during data acquisition and the noisy edges occur at the  
15  
16 end of the scanning line. Thus, the calculated rotation and strain maps presented are largely raw  
17  
18 and unfiltered.  
19  
20  
21  
22

23  
24 We define  $\mathbf{w}$  as the probe scanning direction and  $\mathbf{v}$  as the direction the probe moves to start  
25  
26 the next row. For the data presented in Figure 6, we used a ~40 nm step size for both  $\mathbf{w}$  and  $\mathbf{v}$   
27  
28 with 128x128 probe positions. From Figure 6a, we notice that only regions closest to the  
29  
30 indentation impression have sustained large in-plane lattice rotations, and these regions appear to  
31  
32 be divided into four zones, with each one of opposite sense to the adjacent zone. We find no  
33  
34 large rotation-free areas directly adjacent to the nanoindent impression, as was found in the  
35  
36 previous studies [30, 31]. A significant rotation difference, about 26° in-plane, is measured on  
37  
38 the left side of the indent impression between the two left rotational lobes.  
39  
40  
41  
42

43  
44 The in-plane strain maps in Figure 6b show large sustained strains within the sample, up to  
45  
46 +/- 8% in local regions. We observe large regions of positive strain (dilatation) in  $\epsilon_{xx}/\epsilon_{yy}$   
47  
48 (yellow/red) that extend out from the indent and also regions of negative strain in  $\epsilon_{xx}/\epsilon_{yy}$   
49  
50 (blue/light blue) near the indent tip. In general, these regions of tensile and compressive strain  
51  
52 correlate well with the bright and dark diffraction contrast, respectively, shown in the ADF  
53  
54  
55  
56  
57  
58  
59  
60  
61  
62  
63  
64  
65

1  
2  
3  
4 image of the indent (Figure 4a).<sup>1</sup> The largest compressive strains occur directly beneath the  
5  
6 indenter tip as expected, which are indicated by dark blue zones in the  $\epsilon_{xx}$  and  $\epsilon_{yy}$  maps. This  
7  
8 region adjacent to the indenter tip also sustains the largest shear strains as well, indicated by the  
9  
10 adjacent blue and red zones in the  $\epsilon_{xy}$  map.  
11  
12  
13

14        Within the shear bands, we find the material has also sustained large strains. The arrows in  
15  
16 the  $\epsilon_{xx}/\epsilon_{yy}$  maps in Figure 6b indicate diagonal bands of compressive and tensile strains that  
17  
18 demarcate the positions of the bottom three shear bands (refer to Figure 3c). The regions in  
19  
20 between these shear bands are nominally free of strain, as expected, except we find in the  $\epsilon_{xx}$   
21  
22 map a large region sustaining ~3% compressive strain between the bottom two shear bands. This  
23  
24 region appears to be nominally dislocation free as evidenced by the lack of contrast in the ADF  
25  
26 image of Figure 4a. For this sample, we assume the origin of strain to be mainly due to the  
27  
28 overlap of the strain fields of the generated dislocations, and that any residual elastic strain  
29  
30 would have relaxed during TEM sample preparation. There are a couple of possibilities that  
31  
32 could explain this feature. It is possible some residual compressive strain may have been locked  
33  
34 in due to oxide growth during sample preparation or from the deposition of the protective  
35  
36 platinum layer as either constraint could impede full relaxation of the foil. There may also be  
37  
38 some out-of-plane rotation in this region. It is conceivable that the generated internal defect  
39  
40 structure itself in this region may be responsible for out-of-plane tilt. Such tilting or bending  
41  
42 may change the strain and rotation decomposition such that strain appears to be present here.  
43  
44 This could be true throughout the sample (although we checked that any out-of-plane tilt was  
45  
46  
47  
48  
49  
50  
51  
52  
53  
54  
55  
56

---

57  
58 <sup>1</sup> In keeping with common usage, we refer to positive and negative normal strains as tensile and  
59  
60 compressive, respectively, with the full knowledge of the imprecision of such terminology when  
61  
62 discussing systems with residual stresses.  
63  
64  
65

1  
2  
3  
4 reasonably low), and so the actual strain values given in the maps should not be considered  
5  
6 absolute as they may be larger than actual.  
7

8  
9 To aid in physically interpreting the measured strains, we can calculate an equivalent  
10 deviatoric (Biot) strain directly from the 2x2 stretch matrix  $\mathbf{H}$  as follows. A 3x3 stretch matrix  $\mathbf{H}$   
11 is constructed, where the off-diagonal, out of plane components are assumed to be zero and the  
12  
13  
14  
15  
16  
17  
18  
19  
20  
21  
22  
23  
24  
25  
26  
27  
28  
29  
30  
31  
32  
33  
34  
35  
36  
37  
38  
39  
40  
41  
42  
43  
44  
45  
46  
47  
48  
49  
50  
51  
52  
53  
54  
55  
56  
57  
58  
59  
60  
61  
62  
63  
64  
65  
66  
67  
68  
69  
70  
71  
72  
73  
74  
75  
76  
77  
78  
79  
80  
81  
82  
83  
84  
85  
86  
87  
88  
89  
90  
91  
92  
93  
94  
95  
96  
97  
98  
99  
100  
101  
102  
103  
104  
105  
106  
107  
108  
109  
110  
111  
112  
113  
114  
115  
116  
117  
118  
119  
120  
121  
122  
123  
124  
125  
126  
127  
128  
129  
130  
131  
132  
133  
134  
135  
136  
137  
138  
139  
140  
141  
142  
143  
144  
145  
146  
147  
148  
149  
150  
151  
152  
153  
154  
155  
156  
157  
158  
159  
160  
161  
162  
163  
164  
165  
166  
167  
168  
169  
170  
171  
172  
173  
174  
175  
176  
177  
178  
179  
180  
181  
182  
183  
184  
185  
186  
187  
188  
189  
190  
191  
192  
193  
194  
195  
196  
197  
198  
199  
200  
201  
202  
203  
204  
205  
206  
207  
208  
209  
210  
211  
212  
213  
214  
215  
216  
217  
218  
219  
220  
221  
222  
223  
224  
225  
226  
227  
228  
229  
230  
231  
232  
233  
234  
235  
236  
237  
238  
239  
240  
241  
242  
243  
244  
245  
246  
247  
248  
249  
250  
251  
252  
253  
254  
255  
256  
257  
258  
259  
260  
261  
262  
263  
264  
265  
266  
267  
268  
269  
270  
271  
272  
273  
274  
275  
276  
277  
278  
279  
280  
281  
282  
283  
284  
285  
286  
287  
288  
289  
290  
291  
292  
293  
294  
295  
296  
297  
298  
299  
300  
301  
302  
303  
304  
305  
306  
307  
308  
309  
310  
311  
312  
313  
314  
315  
316  
317  
318  
319  
320  
321  
322  
323  
324  
325  
326  
327  
328  
329  
330  
331  
332  
333  
334  
335  
336  
337  
338  
339  
340  
341  
342  
343  
344  
345  
346  
347  
348  
349  
350  
351  
352  
353  
354  
355  
356  
357  
358  
359  
360  
361  
362  
363  
364  
365  
366  
367  
368  
369  
370  
371  
372  
373  
374  
375  
376  
377  
378  
379  
380  
381  
382  
383  
384  
385  
386  
387  
388  
389  
390  
391  
392  
393  
394  
395  
396  
397  
398  
399  
400  
401  
402  
403  
404  
405  
406  
407  
408  
409  
410  
411  
412  
413  
414  
415  
416  
417  
418  
419  
420  
421  
422  
423  
424  
425  
426  
427  
428  
429  
430  
431  
432  
433  
434  
435  
436  
437  
438  
439  
440  
441  
442  
443  
444  
445  
446  
447  
448  
449  
450  
451  
452  
453  
454  
455  
456  
457  
458  
459  
460  
461  
462  
463  
464  
465  
466  
467  
468  
469  
470  
471  
472  
473  
474  
475  
476  
477  
478  
479  
480  
481  
482  
483  
484  
485  
486  
487  
488  
489  
490  
491  
492  
493  
494  
495  
496  
497  
498  
499  
500  
501  
502  
503  
504  
505  
506  
507  
508  
509  
510  
511  
512  
513  
514  
515  
516  
517  
518  
519  
520  
521  
522  
523  
524  
525  
526  
527  
528  
529  
530  
531  
532  
533  
534  
535  
536  
537  
538  
539  
540  
541  
542  
543  
544  
545  
546  
547  
548  
549  
550  
551  
552  
553  
554  
555  
556  
557  
558  
559  
560  
561  
562  
563  
564  
565  
566  
567  
568  
569  
570  
571  
572  
573  
574  
575  
576  
577  
578  
579  
580  
581  
582  
583  
584  
585  
586  
587  
588  
589  
590  
591  
592  
593  
594  
595  
596  
597  
598  
599  
600  
601  
602  
603  
604  
605  
606  
607  
608  
609  
610  
611  
612  
613  
614  
615  
616  
617  
618  
619  
620  
621  
622  
623  
624  
625  
626  
627  
628  
629  
630  
631  
632  
633  
634  
635  
636  
637  
638  
639  
640  
641  
642  
643  
644  
645  
646  
647  
648  
649  
650  
651  
652  
653  
654  
655  
656  
657  
658  
659  
660  
661  
662  
663  
664  
665  
666  
667  
668  
669  
670  
671  
672  
673  
674  
675  
676  
677  
678  
679  
680  
681  
682  
683  
684  
685  
686  
687  
688  
689  
690  
691  
692  
693  
694  
695  
696  
697  
698  
699  
700  
701  
702  
703  
704  
705  
706  
707  
708  
709  
710  
711  
712  
713  
714  
715  
716  
717  
718  
719  
720  
721  
722  
723  
724  
725  
726  
727  
728  
729  
730  
731  
732  
733  
734  
735  
736  
737  
738  
739  
740  
741  
742  
743  
744  
745  
746  
747  
748  
749  
750  
751  
752  
753  
754  
755  
756  
757  
758  
759  
760  
761  
762  
763  
764  
765  
766  
767  
768  
769  
770  
771  
772  
773  
774  
775  
776  
777  
778  
779  
780  
781  
782  
783  
784  
785  
786  
787  
788  
789  
790  
791  
792  
793  
794  
795  
796  
797  
798  
799  
800  
801  
802  
803  
804  
805  
806  
807  
808  
809  
810  
811  
812  
813  
814  
815  
816  
817  
818  
819  
820  
821  
822  
823  
824  
825  
826  
827  
828  
829  
830  
831  
832  
833  
834  
835  
836  
837  
838  
839  
840  
841  
842  
843  
844  
845  
846  
847  
848  
849  
850  
851  
852  
853  
854  
855  
856  
857  
858  
859  
860  
861  
862  
863  
864  
865  
866  
867  
868  
869  
870  
871  
872  
873  
874  
875  
876  
877  
878  
879  
880  
881  
882  
883  
884  
885  
886  
887  
888  
889  
890  
891  
892  
893  
894  
895  
896  
897  
898  
899  
900  
901  
902  
903  
904  
905  
906  
907  
908  
909  
910  
911  
912  
913  
914  
915  
916  
917  
918  
919  
920  
921  
922  
923  
924  
925  
926  
927  
928  
929  
930  
931  
932  
933  
934  
935  
936  
937  
938  
939  
940  
941  
942  
943  
944  
945  
946  
947  
948  
949  
950  
951  
952  
953  
954  
955  
956  
957  
958  
959  
960  
961  
962  
963  
964  
965  
966  
967  
968  
969  
970  
971  
972  
973  
974  
975  
976  
977  
978  
979  
980  
981  
982  
983  
984  
985  
986  
987  
988  
989  
990  
991  
992  
993  
994  
995  
996  
997  
998  
999  
1000

To aid in physically interpreting the measured strains, we can calculate an equivalent deviatoric (Biot) strain directly from the 2x2 stretch matrix  $\mathbf{H}$  as follows. A 3x3 stretch matrix  $\mathbf{H}$  is constructed, where the off-diagonal, out of plane components are assumed to be zero and the zz-diagonal component is taken to be the inverse of the determinant of the 2x2  $\mathbf{H}$  matrix, i.e. incompressible plastic flow. The 3x3 strain matrix,  $\mathbf{E}$ , is computed from  $\mathbf{H}$ , and finally we take the norm of this finite strain deviatoric matrix and multiply by  $\sqrt{2/3}$ . The result, given in Figure 6c, can be interpreted as an equivalent deviatoric (Biot) strain measure using an assumption of incompressibility. This metric should approximate the actual shear strain endured by the sample. This equivalent strain appears physically reasonable through most of the indent and rises steeply in the region directly underneath the indentation apex, as expected. This map thus physically substantiates the measured diffraction data and resultant strain and rotation calculations.

As we are also interested in the continuous lattice rotations beneath the indent, we performed NPD experiments at higher spatial resolutions about the two rotational lobes observed on the left side of the indent, outlined in red in Figure 7a. For the maps in Figure 7, we used a step size in  $w$  and  $v$  of ~40nm with 32x32 probe positions. The rotation map measured from the data is shown in Figure 7b (the indent has been rotated in the image, such that its left boundary lies horizontally).

A bright-field TEM image of one of the lobes, along with its boundary, is shown in Figure 7 and is a higher magnification image of the region outlined in blue in Figure 7a. We observe a dense forest of dislocations is present adjacent to the indent within this lobe and conclude that these dislocations must be responsible for the measured lattice rotations. Due to the constantly

1  
2  
3  
4 changing orientation in this part of the sample, the images (both Figure 7a and c) do contain  
5  
6 regions in which there are no immediately visible dislocations. Upon specimen tilting, however,  
7  
8 we confirm that forest configurations are present in all areas adjacent to the indent impression.  
9  
10 Thus, there is strong evidence suggesting that typical dislocations may be responsible for the  
11  
12 measured continuous lattice rotations.  
13  
14

15  
16 From the given in-plane rotation map (Figure 7b), we can directly quantify the density of  
17  
18 geometrically necessary dislocations required to sustain the measured lattice rotations by  
19  
20 computing Nye's dislocation tensor. Tensor components were computed using a custom Matlab  
21  
22 script based on the derivation by Pantleon (2008), in which the analysis was applied to similar  
23  
24 rotation data acquired from EBSD [32]. For the calculation, we used a Burgers vector of  
25  
26  $2.85 \times 10^{-9} \text{ m} \cdot a_0 / 2 \cdot \langle 111 \rangle$ . Figure 7d gives the  $\alpha_{xz}$  and  $\alpha_{yz}$  components, where the basis vectors  $\mathbf{x}$ ,  
27  
28  $\mathbf{y}$ , and  $\mathbf{z}$  are nominally parallel to the [-1-10], [1-10] and [001] directions, respectively, consistent  
29  
30 with the previous data sets shown. From the dislocation maps, we find the densities associated  
31  
32 with the boundary between the lobes, where the rotation gradient is largest, are  $\sim 10^{15} / \text{m}^2$  for  
33  
34 both  $\alpha_{xz}$  and  $\alpha_{yz}$ . The calculated GND, while large, is not unreasonable for a heavily deformed  
35  
36 material and indicates that the measured rotations displayed in Figure 7b is physically plausible.  
37  
38  
39  
40  
41  
42

43 To further investigate the nature of this large rotation gradient on the side of the indent  
44  
45 (Figure 7b), we performed NPD at an even higher spatial resolution. For the maps in Figure 8a  
46  
47 and b, we used a  $\sim 1 \text{ nm}$  probe size and  $6.7 \times 13.4 \text{ nm}$  step size in **w** and **v** with  $128 \times 32$  probe  
48  
49 positions. Such resolution will allow us to determine whether the boundary between the  
50  
51 rotational lobes is comprised of a discrete, small-angle grain boundary or the rotations are truly  
52  
53 continuous at the nanometer scale. The resulting rotation map is given in Figure 8a and is  
54  
55 superimposed upon the HAADF image of the indent. At the reduced step size used, the lattice  
56  
57  
58  
59  
60  
61  
62  
63  
64  
65

1  
2  
3  
4 rotations appear mostly continuous except right at the junction between the lobe and indent  
5 boundary (yellow). Here, the change in rotation sense appears discrete, in that it changes  
6 substantially over a couple of nm. This boundary region between the rotational lobes was further  
7 analyzed with 128x128 probe positions at a step size in **w and v** of 1.2 nm. The resulting  
8 rotational map is given in the Figure 8a inset. Interestingly, the boundary between the adjacent  
9 lobes appears discrete on the upper right near the nanoindent boundary, jumping from 3° to -6°  
10 within a couple of nm. Such a large, discrete rotational jump, ~9°, indicates possible low-angle  
11 grain boundary formation. However, this discrete interface quickly becomes more diffuse away  
12 from the indentation boundary. Thus, it appears that the boundary between these lobes of  
13 opposite rotational sense are largely continuous in nature at the nm scale.

14  
15  
16  
17  
18  
19  
20  
21  
22  
23  
24  
25  
26  
27  
28  
29 The corresponding strain maps associated with this data set are given in Figure 8b, which use  
30 the same x-y coordinate system defined in Figure 6b. In general, there are positive tensile strains  
31 of ~ 2-3% in both the x and y directions throughout the region. Further, it appears that larger  
32 strains (~ 6-9%) are endured on the right side of the  $\epsilon_{xx}$  map and on the left side of the  $\epsilon_{yy}$  map.  
33  
34  
35  
36  
37  
38  
39  
40  
41  
42  
43  
44  
45  
46  
47  
48  
49  
50  
51  
52  
53  
54  
55  
56  
57  
58  
59  
60  
61  
62  
63  
64  
65  
66  
67  
68  
69  
70  
71  
72  
73  
74  
75  
76  
77  
78  
79  
80  
81  
82  
83  
84  
85  
86  
87  
88  
89  
90  
91  
92  
93  
94  
95  
96  
97  
98  
99  
100  
101  
102  
103  
104  
105  
106  
107  
108  
109  
110  
111  
112  
113  
114  
115  
116  
117  
118  
119  
120  
121  
122  
123  
124  
125  
126  
127  
128  
129  
130  
131  
132  
133  
134  
135  
136  
137  
138  
139  
140  
141  
142  
143  
144  
145  
146  
147  
148  
149  
150  
151  
152  
153  
154  
155  
156  
157  
158  
159  
160  
161  
162  
163  
164  
165  
166  
167  
168  
169  
170  
171  
172  
173  
174  
175  
176  
177  
178  
179  
180  
181  
182  
183  
184  
185  
186  
187  
188  
189  
190  
191  
192  
193  
194  
195  
196  
197  
198  
199  
200  
201  
202  
203  
204  
205  
206  
207  
208  
209  
210  
211  
212  
213  
214  
215  
216  
217  
218  
219  
220  
221  
222  
223  
224  
225  
226  
227  
228  
229  
230  
231  
232  
233  
234  
235  
236  
237  
238  
239  
240  
241  
242  
243  
244  
245  
246  
247  
248  
249  
250  
251  
252  
253  
254  
255  
256  
257  
258  
259  
260  
261  
262  
263  
264  
265  
266  
267  
268  
269  
270  
271  
272  
273  
274  
275  
276  
277  
278  
279  
280  
281  
282  
283  
284  
285  
286  
287  
288  
289  
290  
291  
292  
293  
294  
295  
296  
297  
298  
299  
300  
301  
302  
303  
304  
305  
306  
307  
308  
309  
310  
311  
312  
313  
314  
315  
316  
317  
318  
319  
320  
321  
322  
323  
324  
325  
326  
327  
328  
329  
330  
331  
332  
333  
334  
335  
336  
337  
338  
339  
340  
341  
342  
343  
344  
345  
346  
347  
348  
349  
350  
351  
352  
353  
354  
355  
356  
357  
358  
359  
360  
361  
362  
363  
364  
365  
366  
367  
368  
369  
370  
371  
372  
373  
374  
375  
376  
377  
378  
379  
380  
381  
382  
383  
384  
385  
386  
387  
388  
389  
390  
391  
392  
393  
394  
395  
396  
397  
398  
399  
400  
401  
402  
403  
404  
405  
406  
407  
408  
409  
410  
411  
412  
413  
414  
415  
416  
417  
418  
419  
420  
421  
422  
423  
424  
425  
426  
427  
428  
429  
430  
431  
432  
433  
434  
435  
436  
437  
438  
439  
440  
441  
442  
443  
444  
445  
446  
447  
448  
449  
450  
451  
452  
453  
454  
455  
456  
457  
458  
459  
460  
461  
462  
463  
464  
465  
466  
467  
468  
469  
470  
471  
472  
473  
474  
475  
476  
477  
478  
479  
480  
481  
482  
483  
484  
485  
486  
487  
488  
489  
490  
491  
492  
493  
494  
495  
496  
497  
498  
499  
500  
501  
502  
503  
504  
505  
506  
507  
508  
509  
510  
511  
512  
513  
514  
515  
516  
517  
518  
519  
520  
521  
522  
523  
524  
525  
526  
527  
528  
529  
530  
531  
532  
533  
534  
535  
536  
537  
538  
539  
540  
541  
542  
543  
544  
545  
546  
547  
548  
549  
550  
551  
552  
553  
554  
555  
556  
557  
558  
559  
560  
561  
562  
563  
564  
565  
566  
567  
568  
569  
570  
571  
572  
573  
574  
575  
576  
577  
578  
579  
580  
581  
582  
583  
584  
585  
586  
587  
588  
589  
590  
591  
592  
593  
594  
595  
596  
597  
598  
599  
600  
601  
602  
603  
604  
605  
606  
607  
608  
609  
610  
611  
612  
613  
614  
615  
616  
617  
618  
619  
620  
621  
622  
623  
624  
625  
626  
627  
628  
629  
630  
631  
632  
633  
634  
635  
636  
637  
638  
639  
640  
641  
642  
643  
644  
645  
646  
647  
648  
649  
650  
651  
652  
653  
654  
655  
656  
657  
658  
659  
660  
661  
662  
663  
664  
665  
666  
667  
668  
669  
670  
671  
672  
673  
674  
675  
676  
677  
678  
679  
680  
681  
682  
683  
684  
685  
686  
687  
688  
689  
690  
691  
692  
693  
694  
695  
696  
697  
698  
699  
700  
701  
702  
703  
704  
705  
706  
707  
708  
709  
710  
711  
712  
713  
714  
715  
716  
717  
718  
719  
720  
721  
722  
723  
724  
725  
726  
727  
728  
729  
730  
731  
732  
733  
734  
735  
736  
737  
738  
739  
740  
741  
742  
743  
744  
745  
746  
747  
748  
749  
750  
751  
752  
753  
754  
755  
756  
757  
758  
759  
760  
761  
762  
763  
764  
765  
766  
767  
768  
769  
770  
771  
772  
773  
774  
775  
776  
777  
778  
779  
780  
781  
782  
783  
784  
785  
786  
787  
788  
789  
790  
791  
792  
793  
794  
795  
796  
797  
798  
799  
800  
801  
802  
803  
804  
805  
806  
807  
808  
809  
810  
811  
812  
813  
814  
815  
816  
817  
818  
819  
820  
821  
822  
823  
824  
825  
826  
827  
828  
829  
830  
831  
832  
833  
834  
835  
836  
837  
838  
839  
840  
841  
842  
843  
844  
845  
846  
847  
848  
849  
850  
851  
852  
853  
854  
855  
856  
857  
858  
859  
860  
861  
862  
863  
864  
865  
866  
867  
868  
869  
870  
871  
872  
873  
874  
875  
876  
877  
878  
879  
880  
881  
882  
883  
884  
885  
886  
887  
888  
889  
890  
891  
892  
893  
894  
895  
896  
897  
898  
899  
900  
901  
902  
903  
904  
905  
906  
907  
908  
909  
910  
911  
912  
913  
914  
915  
916  
917  
918  
919  
920  
921  
922  
923  
924  
925  
926  
927  
928  
929  
930  
931  
932  
933  
934  
935  
936  
937  
938  
939  
940  
941  
942  
943  
944  
945  
946  
947  
948  
949  
950  
951  
952  
953  
954  
955  
956  
957  
958  
959  
960  
961  
962  
963  
964  
965  
966  
967  
968  
969  
970  
971  
972  
973  
974  
975  
976  
977  
978  
979  
980  
981  
982  
983  
984  
985  
986  
987  
988  
989  
990  
991  
992  
993  
994  
995  
996  
997  
998  
999  
1000

#### 4. Discussion

The three intriguing aspects of the deformation of STGM under nanoindentation that motivate this study involve understanding the defect structure within the seemingly featureless nanoindentation pit, the exact nature of the continuous rotations comprising this region, and the severe dislocation bowing surrounding the indent pit that indicated the presence of structural obstacles. With respect to the questions regarding the indentation pit, we have been able to

1  
2  
3  
4 quantify the lattice rotations and find a physically reasonable dislocation density that may be  
5 accommodated. Correlative bright field TEM imaging confirms the presence of very dense,  
6  
7 complex dislocation structures likely mediating these rotations. We also find that dislocations  
8  
9 outside the indent pit, while remaining elusive to directly image or observe, particularly if small  
10  
11 or oriented unfavorably, can serve as potent barriers to the motion of other dislocations.  
12  
13  
14 Previous studies have observed dislocation motion being hindered, both directly [12] and  
15  
16 indirectly [4], and it has been speculated that atomic-scale embryos of  $\omega$  phase or ZrO clusters  
17  
18 could be responsible. Here we argue that dislocations themselves may very well have been  
19  
20 effective obstacles in these cases.  
21  
22  
23  
24

25  
26 In pursuing this in-depth investigation, additional intriguing observations emerged involving  
27  
28 specific dislocation arrangements along with a lack of other intruding deformation mechanisms,  
29  
30 shear banding, and the presence of rotational lobes in the pit. These features are also addressed  
31  
32 in detail in the following sections.  
33  
34

#### 35 36 4.1. Dislocation-mediated plasticity in STGMs 37

38  
39 The main results from TEM imaging demonstrate that the deformation behavior of STGM  
40  
41 under nanoindentation appears to be solely governed by  $a/2\langle 111 \rangle$ -type dislocation glide on both  
42  
43 the  $\{110\}$  and  $\{112\}$  plane families (Figure 3). We note that no secondary spots were observed  
44  
45 in the raw diffraction data in this study. The observation of a plastic deformation mechanism  
46  
47 involving only dislocation slip in gum metals is not typical. Of course, the original paper on  
48  
49 gum metal by Saito et al [4] claimed a dislocation-free ideal shear deformation mechanism  
50  
51 mediated by giant faults formed via nanodisturbance generation, which seemed to be supported  
52  
53 by the results of mechanical testing in which gum metal exhibited a lack of work hardening [4,  
54  
55  
56  
57  
58 27] and a tensile strength near its ideal value [4] given the measured elastic constants available at  
59  
60  
61  
62  
63  
64  
65



1  
2  
3  
4 the time [33,34].<sup>2,[35,36]</sup>. However, more recent studies of gum metals have typically observed a  
5  
6 mix of dislocation slip, stress-induced phase transformations, and mechanical twinning upon  
7  
8 deformation. Specifically, a combination of deformation induced  $\omega$  or martensitic  $\alpha''$ , twinning,  
9  
10 and slip band formation have been observed in uniaxial tension [15], compression [14, 17], and  
11  
12 in elastic load cycling of STGMs [16]. Yet, in each of these studies, dislocation slip either  
13  
14 coexisted with these mechanisms or simply did not play a significant role, if any at all. Few  
15  
16 other studies have claimed a sole dislocation slip-based plasticity mechanism [12, 13] for  
17  
18 STGMs, as we do.  
19  
20  
21  
22

23  
24 The remaining question in this study is, given that typical BCC twinning modes and stress-  
25  
26 induced  $\omega$  have been observed in as-received CWGM samples [37, 10] and upon deformation of  
27  
28 STGMs [14, 15], “why we would fail to observe them here?” Firstly, it is well known that the  
29  
30 operating deformation mechanism of Beta-Ti alloys is extremely sensitive to the stability of the  
31  
32 beta phase [38, 39]. Beta-Ti stability can be empirically quantified by the Molybdenum  
33  
34 equivalent ( $Mo_{eq}$  metric) [40], where the alloy is considered stable against martensitic  
35  
36 transformation roughly above a  $Mo_{eq}$  value of 10. The gum metal used in the present study did  
37  
38 not appear to contain any athermal  $\omega$  ( $\omega_{ath}$ ) phase after solution treatment and final quench,  
39  
40 consistent with its  $Mo_{eq}$  value of 10.49. In a uniaxial tension experiment of cast STGM by  
41  
42 Plancher et al. [15] deformation-induced  $\omega$  and  $\langle 111 \rangle \{ 112 \}$  twinning was observed, but the  
43  
44 sample initially contained  $\omega_{ath}$  upon quench implying an intrinsic beta-instability consistent with  
45  
46 its lower  $Mo_{eq}$  value of 10.27. Similarly, Yang et al. [14] demonstrated under uniaxial  
47  
48 compression that  $\langle 111 \rangle \{ 112 \}$ ,  $\langle 113 \rangle \{ 332 \}$  twinning and deformation-induced  $\omega$  coexisted with  
49  
50  
51  
52  
53  
54  
55  
56

---

57  
58 <sup>2</sup> We note that a lack of work hardening in tensile curves is likely typical of many Ti alloys,  
59 especially  $\beta$ -Ti 27 alloys [35], and that the ideal strength was later recalculated via  
60 experimentally determined elastic constants to be roughly double the tensile strength [36].  
61  
62  
63  
64  
65

1  
2  
3  
4 dislocation slip for their STGM, also consistent with its lower  $M_{o_{eq}}$  of 10.34. While these values  
5  
6 may appear relatively close to that of the present alloy, the composition of gum metals has been  
7  
8 specifically engineered to lie right on the edge of beta stability, and it seems reasonable that  
9  
10 deviation of this parameter towards instability could drastically change the dominant  
11  
12 deformation mechanism. Specifically, the mechanism of mechanical twinning and  $\omega$   
13  
14 transformation is thought to be directly aided by structural instability of the BCC lattice.  $\langle 111 \rangle$   
15  
16  $\{112\}$  twinning can be realized through  $a/6\langle 111 \rangle$  shear on successive  $\{112\}$  planes. Similarly,  
17  
18 while the  $\beta \rightarrow \omega$  transformation is typically easily understood through a shuffle mechanism  
19  
20 involving the “collapse” of  $\{111\}$ -plane pairs, it may also be described by inhomogeneous shear  
21  
22 in  $\langle 111 \rangle$ -type directions on successive  $\{112\}$  planes [41]. The lower shear modulus in the  
23  
24  $\langle 111 \rangle$  direction induced by decreased  $\beta$ -phase stability will lower the energy barrier for the  
25  
26 shear required by either transformation. Further, the presence of any  $\omega_{ath}$  could also lower the  
27  
28 nucleation barrier for deformation-induced phase transformations compared to an alloy initially  
29  
30 free of secondary phases. Consistent with this reasoning, Castany et al. [12] and Kamimura et  
31  
32 al.[13] tested STGMs with a  $M_{o_{eq}}$  of 10.49 and 10.45, respectively, and observed direct and  
33  
34 indirect evidence, respectively, of dislocation slip only. Some authors of the present study have  
35  
36 in fact performed  $\langle 110 \rangle$  nanoindentation on another specimen provided by Toyota Central R&D  
37  
38 but leaner in Nb, with a lower  $M_{o_{eq}}$  of 9.37 and containing initial  $\omega_{ath}$  precipitates. The results of  
39  
40 this experiment yielded clear  $\langle 111 \rangle\{112\}$  mechanical twins and stress-induced  $\omega$  laths in direct  
41  
42 contrast to the results in this investigation [42].  
43  
44  
45  
46  
47  
48  
49  
50  
51  
52

53  
54 It is clear from these prior studies that other deformation mechanisms can intrude in other  
55  
56 stress states apart from nanoindentation. We simply establish in this study that these mechanisms  
57  
58 are not needed to explain behavior in nanoindentation, and dislocation slip can fully account for  
59  
60  
61  
62  
63  
64  
65

1  
2  
3  
4 defect structures observed here. Still, we are aware that the deformation patterns we have  
5  
6 analyzed are those that exist post-indentation. It remains possible that other deformation modes  
7  
8 intrude during the indentation itself, which evolve into dislocation configurations as the system  
9  
10 relaxes after deformation. This seems unlikely, with the possible exception of the shear bands,  
11  
12 since the dislocation patterns are obviously compatible with the overall deformation imposed by  
13  
14 the indent.  
15  
16  
17  
18

#### 19 4.2. On Giant Fault mechanism

20  
21 Also found in this study were highly localized regions of plastic deformation occurring  
22  
23 within shear bands on the  $\langle 111 \rangle \{-1-12\}$  slip system (Figure 3b), some of which contained  
24  
25 dislocation cell networks. These shear bands appeared as isolated regions surrounded by swaths  
26  
27 of un-deformed material, very similar to the “giant fault” structures reported for deformed gum  
28  
29 metals [4, 8]. In the present study, we found the shear bands lie on the  $\{112\}$ -type plane.  
30  
31 Similarly, Kuramoto et al. [8] observed that the giant faults in STGMs after tensile testing also  
32  
33 lied close to  $\{112\}$ -type planes, specifically rotated  $13^\circ$  away from  $[111]$  (1-1-2) about the  $[110]$   
34  
35 direction and oriented  $\sim 45^\circ$  to the tensile axis. However, they did not observe any discrete  
36  
37 dislocations within the faults, only local lattice rotations surrounding them. The orientation of  
38  
39 the faults as  $45^\circ$  from the tensile axis without the presence of dislocation structures seemingly  
40  
41 supported the theory that gum metals deform via ideal shear. Further, first principles calculations  
42  
43 of elastic constants in gum metal approximants detailed how an applied shear oriented  $\sim 13^\circ$  from  
44  
45  $\langle 111 \rangle (1-1-2)$  about the  $[110]$  direction can allow, with help from a particular soft phonon mode  
46  
47 in gum metals to aid atomic shuffle, for transformation to the HCP structure [43]. This structural  
48  
49 transformation as a deformation mechanism could further explain the lack of dislocation  
50  
51 evidence near the giant faults (although, no secondary phases were observed in the original  
52  
53  
54  
55  
56  
57  
58  
59  
60  
61  
62  
63  
64  
65

1  
2  
3  
4 studies). In the present study, however, we have clear evidence that the motion of dislocations  
5  
6 with  $\mathbf{b}$  of  $\langle -111 \rangle$ -type is responsible for the shear bands observed on the  $\{112\}$  planes.  
7  
8

9 A few possibilities can explain the differences between our and prior studies with respect to  
10  
11 giant faults and shear bands. First, it is possible that actual dislocations were present in the giant  
12  
13 faults: the prior studies prepared samples to view faults along their traces, and in our study, we  
14  
15 view the projection of the face of the shear band allowing clear visualization of the structures  
16  
17 from which they are comprised. On the other hand, our study involved compression via  
18  
19 nanoindentation, and it is possible that any ideal shearing mechanism may have been suppressed  
20  
21 by surrounding material constraints, whereas in a tensile test, the giant faults could propagate  
22  
23 easily through the material to free, unconstrained, surfaces. These free surfaces allow for the  
24  
25 deformed material within the faults to protrude above the original surface, as clearly seen in  
26  
27 images in Ref. [8].  
28  
29  
30  
31  
32

### 33 4.3. Nanoindentation-induced lattice rotations 34

35 One of our original questions was whether the large lattice rotations, as observed  
36  
37 qualitatively in nanoindented STGM [22], were continuous and could be accommodated by a  
38  
39 reasonable quantity of dislocations. The dislocation density calculated from the NPD data linked  
40  
41 with the dense forest of dislocations explains the origin of severe rotations, previously observed  
42  
43 under nanoindentation, to be conventional slip (Figure 7c, d). In quantifying the rotation, we  
44  
45 found rotational lobes of opposite sense adjacent to each other. **Prior studies utilizing the EBSD**  
46  
47 **technique have also observed large crystal reorientation zones as well. Table 2 presents a**  
48  
49 **summary of these studies (Refs. [30, 31, 44, 45]) along with the current investigation.** It is noted  
50  
51 that there is no readily available prior study for BCC materials and comparison is made with  
52  
53  
54  
55  
56  
57  
58  
59  
60  
61  
62  
63  
64  
65  
66  
67  
68  
69  
70  
71  
72  
73  
74  
75  
76  
77  
78  
79  
80  
81  
82  
83  
84  
85  
86  
87  
88  
89  
90  
91  
92  
93  
94  
95  
96  
97  
98  
99  
100  
101  
102  
103  
104  
105  
106  
107  
108  
109  
110  
111  
112  
113  
114  
115  
116  
117  
118  
119  
120  
121  
122  
123  
124  
125  
126  
127  
128  
129  
130  
131  
132  
133  
134  
135  
136  
137  
138  
139  
140  
141  
142  
143  
144  
145  
146  
147  
148  
149  
150  
151  
152  
153  
154  
155  
156  
157  
158  
159  
160  
161  
162  
163  
164  
165  
166  
167  
168  
169  
170  
171  
172  
173  
174  
175  
176  
177  
178  
179  
180  
181  
182  
183  
184  
185  
186  
187  
188  
189  
190  
191  
192  
193  
194  
195  
196  
197  
198  
199  
200  
201  
202  
203  
204  
205  
206  
207  
208  
209  
210  
211  
212  
213  
214  
215  
216  
217  
218  
219  
220  
221  
222  
223  
224  
225  
226  
227  
228  
229  
230  
231  
232  
233  
234  
235  
236  
237  
238  
239  
240  
241  
242  
243  
244  
245  
246  
247  
248  
249  
250  
251  
252  
253  
254  
255  
256  
257  
258  
259  
260  
261  
262  
263  
264  
265  
266  
267  
268  
269  
270  
271  
272  
273  
274  
275  
276  
277  
278  
279  
280  
281  
282  
283  
284  
285  
286  
287  
288  
289  
290  
291  
292  
293  
294  
295  
296  
297  
298  
299  
300  
301  
302  
303  
304  
305  
306  
307  
308  
309  
310  
311  
312  
313  
314  
315  
316  
317  
318  
319  
320  
321  
322  
323  
324  
325  
326  
327  
328  
329  
330  
331  
332  
333  
334  
335  
336  
337  
338  
339  
340  
341  
342  
343  
344  
345  
346  
347  
348  
349  
350  
351  
352  
353  
354  
355  
356  
357  
358  
359  
360  
361  
362  
363  
364  
365  
366  
367  
368  
369  
370  
371  
372  
373  
374  
375  
376  
377  
378  
379  
380  
381  
382  
383  
384  
385  
386  
387  
388  
389  
390  
391  
392  
393  
394  
395  
396  
397  
398  
399  
400  
401  
402  
403  
404  
405  
406  
407  
408  
409  
410  
411  
412  
413  
414  
415  
416  
417  
418  
419  
420  
421  
422  
423  
424  
425  
426  
427  
428  
429  
430  
431  
432  
433  
434  
435  
436  
437  
438  
439  
440  
441  
442  
443  
444  
445  
446  
447  
448  
449  
450  
451  
452  
453  
454  
455  
456  
457  
458  
459  
460  
461  
462  
463  
464  
465  
466  
467  
468  
469  
470  
471  
472  
473  
474  
475  
476  
477  
478  
479  
480  
481  
482  
483  
484  
485  
486  
487  
488  
489  
490  
491  
492  
493  
494  
495  
496  
497  
498  
499  
500  
501  
502  
503  
504  
505  
506  
507  
508  
509  
510  
511  
512  
513  
514  
515  
516  
517  
518  
519  
520  
521  
522  
523  
524  
525  
526  
527  
528  
529  
530  
531  
532  
533  
534  
535  
536  
537  
538  
539  
540  
541  
542  
543  
544  
545  
546  
547  
548  
549  
550  
551  
552  
553  
554  
555  
556  
557  
558  
559  
560  
561  
562  
563  
564  
565  
566  
567  
568  
569  
570  
571  
572  
573  
574  
575  
576  
577  
578  
579  
580  
581  
582  
583  
584  
585  
586  
587  
588  
589  
590  
591  
592  
593  
594  
595  
596  
597  
598  
599  
600  
601  
602  
603  
604  
605  
606  
607  
608  
609  
610  
611  
612  
613  
614  
615  
616  
617  
618  
619  
620  
621  
622  
623  
624  
625  
626  
627  
628  
629  
630  
631  
632  
633  
634  
635  
636  
637  
638  
639  
640  
641  
642  
643  
644  
645  
646  
647  
648  
649  
650  
651  
652  
653  
654  
655  
656  
657  
658  
659  
660  
661  
662  
663  
664  
665  
666  
667  
668  
669  
670  
671  
672  
673  
674  
675  
676  
677  
678  
679  
680  
681  
682  
683  
684  
685  
686  
687  
688  
689  
690  
691  
692  
693  
694  
695  
696  
697  
698  
699  
700  
701  
702  
703  
704  
705  
706  
707  
708  
709  
710  
711  
712  
713  
714  
715  
716  
717  
718  
719  
720  
721  
722  
723  
724  
725  
726  
727  
728  
729  
730  
731  
732  
733  
734  
735  
736  
737  
738  
739  
740  
741  
742  
743  
744  
745  
746  
747  
748  
749  
750  
751  
752  
753  
754  
755  
756  
757  
758  
759  
760  
761  
762  
763  
764  
765  
766  
767  
768  
769  
770  
771  
772  
773  
774  
775  
776  
777  
778  
779  
780  
781  
782  
783  
784  
785  
786  
787  
788  
789  
790  
791  
792  
793  
794  
795  
796  
797  
798  
799  
800  
801  
802  
803  
804  
805  
806  
807  
808  
809  
810  
811  
812  
813  
814  
815  
816  
817  
818  
819  
820  
821  
822  
823  
824  
825  
826  
827  
828  
829  
830  
831  
832  
833  
834  
835  
836  
837  
838  
839  
840  
841  
842  
843  
844  
845  
846  
847  
848  
849  
850  
851  
852  
853  
854  
855  
856  
857  
858  
859  
860  
861  
862  
863  
864  
865  
866  
867  
868  
869  
870  
871  
872  
873  
874  
875  
876  
877  
878  
879  
880  
881  
882  
883  
884  
885  
886  
887  
888  
889  
890  
891  
892  
893  
894  
895  
896  
897  
898  
899  
900  
901  
902  
903  
904  
905  
906  
907  
908  
909  
910  
911  
912  
913  
914  
915  
916  
917  
918  
919  
920  
921  
922  
923  
924  
925  
926  
927  
928  
929  
930  
931  
932  
933  
934  
935  
936  
937  
938  
939  
940  
941  
942  
943  
944  
945  
946  
947  
948  
949  
950  
951  
952  
953  
954  
955  
956  
957  
958  
959  
960  
961  
962  
963  
964  
965  
966  
967  
968  
969  
970  
971  
972  
973  
974  
975  
976  
977  
978  
979  
980  
981  
982  
983  
984  
985  
986  
987  
988  
989  
990  
991  
992  
993  
994  
995  
996  
997  
998  
999  
1000

1  
2  
3  
4 indent is likely due to slip. Most studies observe rotation free areas between the zones, whereas  
5  
6 we find they are immediately adjacent to each other. Other features that we observe, including  
7  
8 small-angle grain boundaries, are consistent with those found in previous studies. Our study is  
9  
10 distinguished from previous ones in that we investigated a BCC metal using the TEM-NPD  
11  
12 technique to demonstrate, for the first time, the truly continuous nature of these rotations at the  
13  
14 nanoscale utilizing a step size of 1.2nm. While the continuous lattice rotations are not  
15  
16 necessarily unique to gum metal, or BCC materials, perhaps the range, spatial extent and  
17  
18 character of the rotational lobes may be. Our analysis further revealed that the dislocation and  
19  
20 slip structures further from the indent had a specific arrangement. The observation of shear bands  
21  
22 and the determination of the character of dislocations comprising them is also unique to this  
23  
24 study.  
25  
26  
27  
28  
29  
30

## 31 32 **5. Conclusions**

33  
34 Extensive characterization of a FIB lift-out cross section of a nanoindented STGM sample  
35  
36 was performed. From conventional TEM analysis, including “g•b” analysis, ADF imaging, and  
37  
38 the powerful nanoprobe diffraction technique, we conclude the following:  
39  
40

- 41  
42 • The deformation in and around the indentation pit can be fully explained by the dense,  
43  
44 complex distribution of dislocations that is revealed by these modern techniques. The  
45  
46 only defects observed are dislocations groups on slip systems typical of BCC materials:  
47  
48  $\langle -111 \rangle \{110\}$  and  $\langle 111 \rangle \{-1-12\}$ . No second-phase particles or twins appear, though  
49  
50 there are regions of highly localized plastic deformation in which the dislocations are  
51  
52 organized into shear bands on  $\{112\}$ -type planes that resemble the “giant faults”  
53  
54 previously observed in tensile-loaded STGMs.  
55  
56  
57  
58  
59  
60  
61  
62  
63  
64  
65

- 1  
2  
3  
4  
5  
6  
7  
8  
9  
10  
11  
12  
13  
14  
15  
16  
17  
18  
19  
20  
21  
22  
23  
24  
25  
26  
27  
28  
29  
30  
31  
32  
33  
34  
35
- Nanoprobe diffraction using steps sizes as small as 1.2nm shows that the lattice rotations found near the center of the pit in prior work are real and truly continuous. However, the pit centers are not devoid of defects. They contain a very high density of dislocations, which are, apparently, the “geometrically necessary dislocations” that produce the lattice rotation. The required dislocation density is near  $10^{15}/\text{m}^2$ , which is very high, but not unreasonable.
  - The local obstacles that strongly pin mobile dislocations in the periphery of the pit are not nanoparticles, but are forest dislocations. Their crystallography is characterized and explained.
  - The deformation accomplished by nanoindentation in solution treated gum metal is due to a dense distribution of dislocations that are normal in BCC metals. While this is the only detailed study known to us of deformation under nanoindentation in a BCC metal, it is entirely possible that the pattern observed here is typical of BCC metals.

## 36 6. Acknowledgments

37  
38  
39  
40  
41  
42  
43

Authors gratefully acknowledge helpful discussions with Thomas C. Pekin on various algorithms for disk position determination in nanoprobe diffraction data.

## 44 7. Funding

45  
46  
47  
48  
49  
50  
51  
52  
53  
54  
55  
56  
57  
58  
59  
60  
61  
62  
63  
64  
65

The authors acknowledge support of the National Science Foundation under Grant Nos. DMR-0706554, DMR-1105081 and Toyota Research and Development. All conventional TEM imaging, NPD STEM imaging and image processing was performed at the Molecular Foundry, supported by the Office of Science, Office of Basic Energy Sciences of the U.S. Department of Energy under Contract No. DE-AC02—05CH11231.

- 1  
2  
3  
4  
5  
6 [1] P. Laheurte, F. Prima, A. Eberhardt, T. Gloriant, M. Wary, E. Patoor, Mechanical properties  
7 of low modulus beta titanium alloys designed from the electronic approach, J. Mech. Behav.  
8 Biomed. Mater. 3 (2010) 565-573.
- 9 [2] M. Niinomi, T. Hattori, K. Morikawa, T. Kasuga, A. Suzuki, H. Fukui and S. Niwa,  
10 Development of low rigidity  $\beta$ -type titanium alloy for biomedical applications, Mater. Trans. 43  
11 (2002) 2970-2977.
- 12 [3] H. Y. Kim, H. Satoru, J.I. Kim, H. Hosoda and S. Miyazaki, Mechanical Properties and  
13 Shape Memory Behavior of Ti-Nb Alloys, Mater. Trans. 45 (2004) 2443-2448.
- 14 [4] T. Saito, T. Furuta, J.H. Hwang, S. Kuramoto, K. Nishino, N. Suzuki, R. Chen, A. Yamada,  
15 K. Ito, Y. Seno, T. Nonaka, H. Ikehata, N. Nagasako, C. Iwamoto, Y. Ikuhara and T. Sakuma,  
16 Multifunctional Alloys Obtained via a Dislocation-Free Plastic Deformation Mechanism,  
17 Science 300 (2003) 464-467.
- 18 [5] C.R. Krenn, D. Roundy, J.W. Morris Jr., M.L. Cohen, Ideal strengths of bcc metals, Mater.  
19 Sci. Eng. A 319–321 (2001) 111–114.
- 20 [6] T. Li, J. W. Morris, Jr., N. Nagasako, S. Kuramoto, D. C. Chrzan, “Ideal” Engineering  
21 Alloys PRL 98 105503 (2007).
- 22 [7] H. Ikehata, N. Nagasako, T. Furuta, A. Fukumoto, K. Miwa, T. Saito, First-principles  
23 calculations for development of low elastic modulus Ti alloys, PRB 70 **174113** (2004).
- 24 [8] S. Kuramoto, T. Furuta, J.H. Hwang, K. Nishino, and T. Saito, Plastic Deformation in a  
25 Multifunctional Ti-Nb-Ta-Zr-O Alloy, Met and Mat Trans A 37A (2006) 657-662.
- 26 [9] M.Y. Gutkin, T. Ishizaki, S. Kuramoto and I.A. Ovid’ko, Nanodisturbances in deformed  
27 Gum Metal, Acta Mater. 54 (2006) 2489-2499.
- 28 [10] R. J. Talling, R. J. Dashwood, M. Jackson, D. Dye, On the mechanism of superelasticity in  
29 Gum metal, Acta Mater. 57 (2009) 1188-1198.
- 30 [11] H. Xing, J. Sun, Q. Yao, W. Y. Guo, R. Chen, Origin of substantial plastic deformation in  
31 Gum Metals , APL 92 **151905** (2008).
- 32 [12] P. Castany, M. Besse, T. Gloriant, Dislocation mobility in gum metal  $\beta$  – titanium alloy  
33 studied via *in situ* transmission electron microscopy, PRB 84 **020201** (2011).
- 34 [13] Y. Kamimura, S. Katakura, K. Edagawa, S. Takeuchi, S. Kuramoto, T. Furuta, Basic  
35 Deformation Mechanism of BCC Titanium-Based Alloy of Gum Metal, Mat. Trans. 57 **9**  
36 (2016) 1526-1534.
- 37 [14] Y. Yang, S. Q. Wu, G. P. Li, Y. L. Li, Y. F. Lu, K. Yang, P. Ge, Evolution of deformation  
38 mechanisms of Ti-22.4Nb-0.73Ta-2Zr-1.34O alloy during straining, Acta Mater. 58 (2010)  
39 2278-2787).
- 40 [15] E. Plancher, C. C. Tasan, S. Sandloebes, D. Raabe, On dislocation involvement in Ti-Nb  
41 gum metal plasticity, Scripta Mater. 68 (2013) 805-808.
- 42 [16] V. A. Vorontsov, N. G. Jones, K. M. Rahman, D. Dye, Superelastic load cycling of Gum  
43 Metal, Acta Mater. 88 (2015) 323-333.
- 44 [17] E. A. Withey, A. M. Minor, D. C. Chrzan, J. W. Morris Jr., S. Kuramoto, The deformation of  
45 Gum Metal through in situ compression of nanopillars, Acta Mater, 58 (2010) 2652-2665.
- 46 [18] J. W. Morris, Jr., Y. Hanlumuang, M. Sherburne, E. Withey, D. C. Chrzan, S. Kuramoto, Y.  
47 Hayashi, M. Hara, Anomalous transformation-induced deformation in  $\langle 110 \rangle$  textured Gum  
48 Metal, Acta Mater. 58 (2010) 3271-2380.
- 49 [19] N. Takesue, Y. Shimizu, T. Yano, M. Hara, S. Kuramoto, J. of Crystal Growth, 311 (2009)  
50 3319-3324.
- 51  
52  
53  
54  
55  
56  
57  
58  
59  
60  
61  
62  
63  
64  
65

- 1  
2  
3  
4  
5  
6 [20] A. M. Minor, S. A. Syed Asif, Z. Shan, E. A. Stach, E. Cyrankowski, T. Wyrobek, and O. L.  
7 Warren, A new view of the onset of plasticity during the nanoindentation of aluminium, *Nature*  
8 *Materials*, 5, (2006), 697-702.
- 9 [21] “Springer Handbook of Experimental Solid Mechanics,” W. N. Sharpe Editor, Springer US  
10 (2008).
- 11 [22] E. Withey, M. Jin, A. Minor, S. Kuramoto, D.C. Chrzan and J.W. Morris, Jr., The  
12 deformation of “Gum Metal” in nanoindentation, *Mat. Sci Eng. A* 493 (2008) 26-42.
- 13 [23] J. Mayer, L. A. Giannuzzi, T. Kamino and J. Michael, TEM Sample Preparation and FIB-  
14 Induced Damage, *MRS Bulletin* 32 (2007) 400-407.
- 15 [24] T. C. Pekin, C. Gammer, J. Ciston, A. M. Minor. C. Ophus, Optimizing disk registration  
16 algorithms for nanobeam electron diffraction strain mapping, *Ultramicroscopy* 176 (2017) 170-  
17 176.
- 18 [25] N. J. Higham, Computing the polar decomposition---with applications, *SIAM J. Sci. Stat.*  
19 *Comput.*, 7(4), 1986, 1164-1174.
- 20 [26] W. C. Oliver and G. M. Pharr, An improved technique for determining hardness and elastic  
21 modulus using load and displacement sensing indentation experiments, *J. Mater. Res.*, 7 No. 6  
22 (1992) 1564-1583.
- 23 [27] T. Saito, T. Furuta, J.H. Hwang, S. Kuramoto, K. Nishino, N. Suzuki, R. Chen, A. Yamada,  
24 K. Ito, Y. Seno, T. Nonaka, H. Ikehata, N. Nagasako, C. Iwamoto, Y. Ikuhara and T. Sakuma,  
25 *Mater. Sci. Forums*, Multifunctional Titanium Alloy “Gum Metal”, 426-424 (2003) 681-688.
- 26 [28] D. Hernandez-Maldonado, H. Yang, L. Jones, R. Groger, P. B. Hirsch, Q. M. Ramasse, P. D.  
27 Nellist, STEM optical sectioning for imaging screw dislocation core structures, The 16<sup>th</sup>  
28 European Microscopy Congress (2016).
- 29 [29] C. Chen, C. Zhu, E. R. White, C. Chiu, M. C. Scott, B. C. Regan, L. D. Marks, Y. Huang, J.  
30 Miao, Three-dimensional imaging of dislocations in a nanoparticle at atomic resolution *Nature*,  
31 496 (2013) 74-77.
- 32 [30] N. Zaafarani, D. Raabe, F. Roters, S. Zaefferer, On the origin of deformation-induced  
33 rotation patterns below nanoindents, *Acta Mater.* **56** (2008) 31-42.
- 34 [31] J. W. Kysar, Y. X. Gan, T. L. Morse, X. Chen, M. E. Jones, High strain gradient plasticity  
35 associated with wedge indentation into face-centered cubic single crystals: Geometrically  
36 necessary dislocation densities, *J. Mech. Phys. Solids* (2007) 1554-1573.
- 37 [32] W. Pantleon, Resolving the geometrically necessary dislocation content by conventional  
38 electron backscattering diffraction, *Scripta Mater.* 58 (2008) p. 994–997.
- 39 [33] T. Li, J. W. Morris, Jr., N. Nagasako, S. Kuramoto, D. C. Chrzan, “Ideal” Engineering  
40 Alloys PRL 98 105503 (2007).
- 41 [34] H. Ikehata, N. Nagasako, T. Furuta, A. Fukumoto, K. Miwa, T. Saito, First-principles  
42 calculations for development of low elastic modulus Ti alloys, *PRB* 70 **174113** (2004).
- 43 [35] “ASM Atlas of Stress-Strain Curves”, ASM International, Materials Park, OH (2002).
- 44 [36] R.J. Talling, R.J. Dashwood, M. Jackson, S. Kuramoto, D. Dye, Determination of ( $C_{11}$  -  
45  $C_{12}$ ) in Ti–36Nb–2Ta–3Zr–0.3O (wt.%) (Gum metal), *Scripta Mater.* 59 (2008) 669-672.
- 46 [37] T. Yano, Y. Murakami, D. Shindo, S. Kuramoto, Study of the nanostructure of Gum Metal  
47 using energy-filtered transmission electron microscopy, *Acta Mater.* **57** (2009) 628-633.
- 48 [38] S. Hanada, O. Izumi, Transmission Electron Microscopic Observations of  
49 Mechanical Twinning in Metastable Beta Titanium Alloys, *Met. Trans. A.* **17A** (1986), p.  
50 1409.
- 51  
52  
53  
54  
55  
56  
57  
58  
59  
60  
61  
62  
63  
64  
65



- 
- 1  
2  
3  
4  
5  
6 [39] S. Ankem, C.A. Greene, Recent developments in microstructure:property relationships  
7 of beta titanium alloys, *Materials Science and Engineering A* **263** (1999) p.127–131.  
8 [40] P.J. Bania, *Beta Titanium Alloys and Their Role in the Titanium Industry JOM*, 46, 16  
9 (1994).  
10 [41] L. M. Hsiung and D. H. Lassila, Shock induced Deformation Twinning and Omega  
11 Transformation in Tantalum and Tantalum-Tungsten Alloys, *Acta Mater* **48** (2000).  
12 [42] R. P. Sankaran, *Deformation Mechanisms of Gum Metals Under Nanoindentation*,  
13 University of California, Berkeley (2015).  
14 [43] Y. Hanlumyuang, R. P. Sankaran, M. P. Sherburne, J. W. Morris Jr., D. C. Chrzan, Phonons  
15 and phase stability in Ti-V approximants to gum metal, *PRB* 85 144108 (2012).  
16 [44] S. J. Lloyd, A. Castellero, F. Giuliani, Y. Long, K. K. McLaughlin, J. M. Molina-  
17 Aldareguia, N. A. Stelmashenko, L. J. Vandeperre and W. J. Clegg. Observations of nanoindents  
18 via cross-sectional transmission electron microscopy: a survey of deformation mechanisms, *Proc.*  
19 *R. Soc. A* 461 (2005) 2521-2543.  
20 [45] M. Rester, C. Motz, R. Pippan, Microstructural investigation of the volume beneath  
21 nanoindentations in copper, *Acta Mater.* 55 (2007) 6427–6435.  
22  
23  
24  
25

26  
27 Figure 1: Schematic of ex-situ lift-out for TEM observation of nanoindentation in cross section  
28 (XS) is provided. (Top) Gum metal cut perpendicular to the swaging axis, which has developed  
29 <110> texture. Nanoindent ROI retrieved via lift-out within dotted rectangle. (Bottom) SEM  
30 image of sample lamella prior to lift-out and final cleaning.  
31

32  
33 Figure 2: Nanoindentation load-displacement curves for STGM sample. Reduced modulus,  $E_r$ , of  
34 91GPa and hardness of 2.63GPa was calculated. No obvious pop-ins observed.  
35

36  
37 Figure 3: Overview bright field TEM images of the nanoindentation cross section. Figures 3a  
38 and 3b are taken at different sample tilts. A variety of defect structures are observed, including  
39 dislocations and small angle grain boundaries (red dotted lines). Highly localized plastic  
40 deformation occurs in shear bands (red arrows). Figures 3c and 3d are images taken with the  
41 given two-beam condition, and four main dislocation groups are present. Example dislocations  
42 from each group outlined: horizontal, “H” (blue), vertical “V” (magenta), Slant up and Slant  
43 Down “SU+SD” (red), and shear bands “SB” (yellow boxes).  
44  
45

46  
47 Figure 4: ADF images of the nanoindent. a) Large density of dislocations and defects are  
48 observed, and the shear bands and dislocation groups previously discussed are apparent. b-d)  
49 Higher magnification images of regions about the indent: b) upper left, c) upper right, and d)  
50 central portion of the indentation area show complex dislocation interactions and entanglement.  
51

52  
53 Figure 5 a) Higher magnification ADF image of the region in Figure 5c, with bowing dislocation  
54 circled b) A defect (arrow) is observed ahead of the cusp of the bowed dislocation. c). Atomic  
55 resolution of this linear defect contains superlattice peaks in between BCC matrix columns. d)  
56 Model of atomic motif within the linear defect, where red is BCC matrix and green denotes the  
57 extra atomic columns. Model shows helicoidal atomic displacements present around a  
58 dislocation core. Linear defect that causes bowing is determined to be mixed dislocation with  $b =$   
59  $a/2 [-1-11]$ , indicating strong, elastic dislocation-dislocation interactions within nanoindent.  
60  
61  
62  
63  
64  
65

1  
2  
3  
4  
5  
6  
7 Figure 6: Nanoprobe diffraction results are given for overview of indent, taken with 128x128  
8 probe positions at a ~40nm step. a) Rotation map is presented, where theta sense is about z-axis,  
9 parallel to [001] direction of reference lattice. Map reveals four rotational lobes of opposite  
10 sense to the adjacent lobe in the immediate vicinity of indent. b) Strain maps with reference axes  
11 given show tensile strains of up to +/-8%. Largest compressive strains occur beneath the  
12 indentation apex. Shear bands have also sustained large strains (arrows). c) An equivalent  
13 deviatoric (Biot) strain measure for the entire indent was calculated and is largest directly  
14 beneath the indentation tip.  
15  
16

17  
18 Figure 7: a) Nanoprobe diffraction was performed within red ROI using 32x32 probe positions  
19 and ~40nm step size. b) Resultant in-plane rotation map shows continuous rotation of ~26° is  
20 sustained near the indent. c) TEM image of the boundary between the two left-most rotational  
21 lobes (blue ROI in a) contains high dislocation density. d)  $\alpha_{xz}$  and  $\alpha_{yz}$  elements of Nye's  
22 dislocation tensor computed from the in-plane rotation map in b) give GND of up to  $\sim 10^{15}/m^2$ .  
23  
24

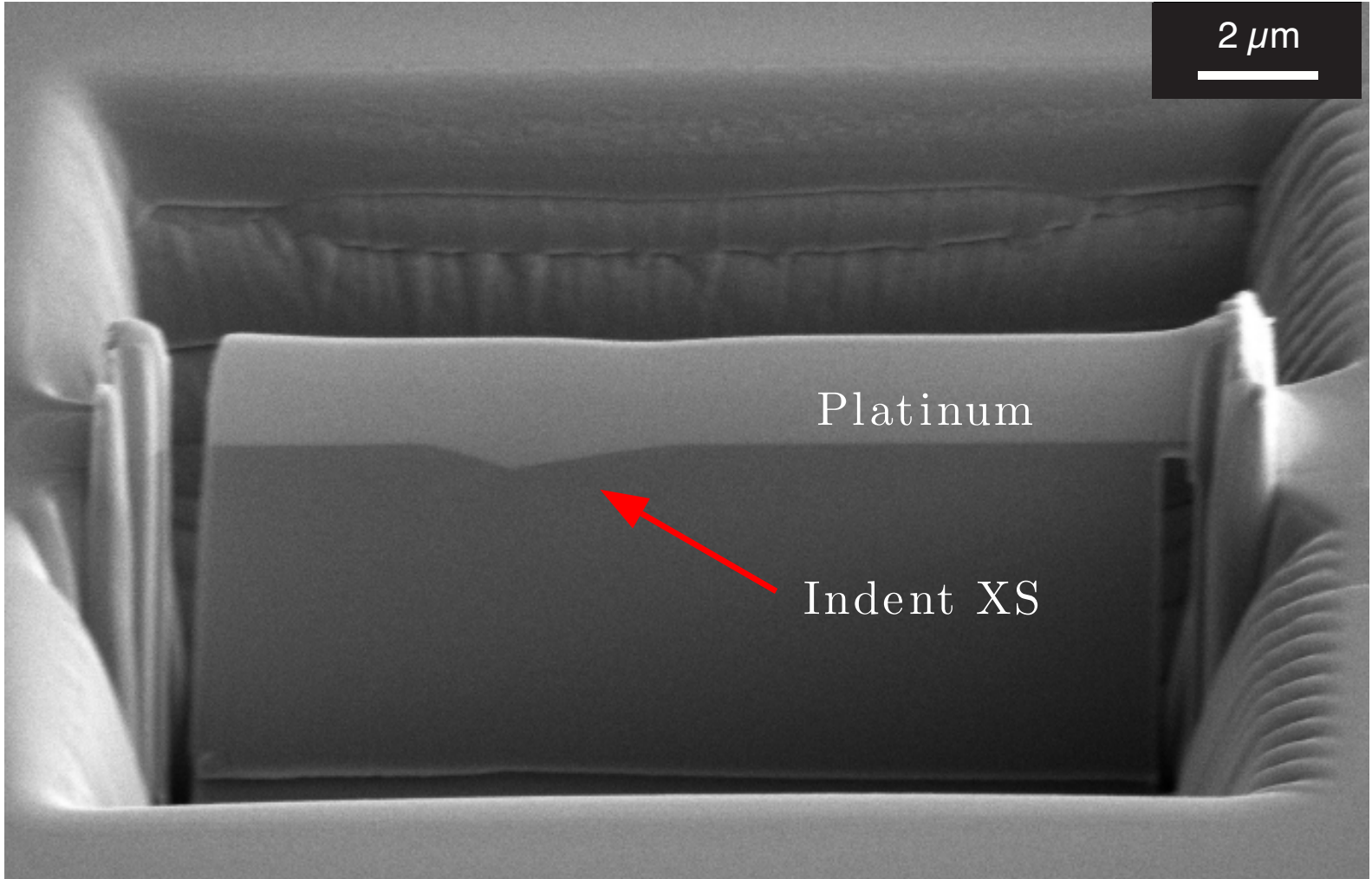
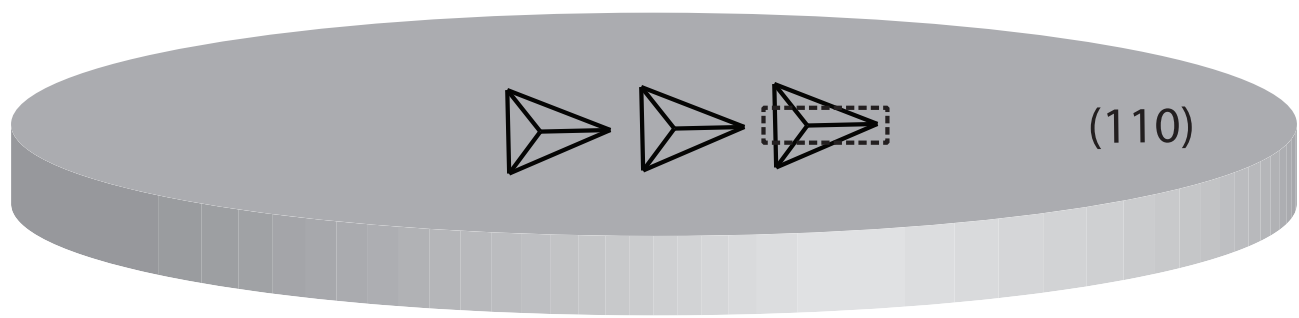
25 Figure 8 a) Rotation map was acquired with 128x32 probe positions at 6.7nm x 13.4nm step size.  
26 (Inset) Region containing boundary was mapped at 128x128 probe positions, 1.2nm step size.  
27 Possible small angle grain boundary is forming adjacent to the indent. Boundary becomes diffuse  
28 away from the indent revealing continuous nature of rotations at the nm-scale. b) Strain maps  
29 show positive tensile strains are present in the region.  
30  
31

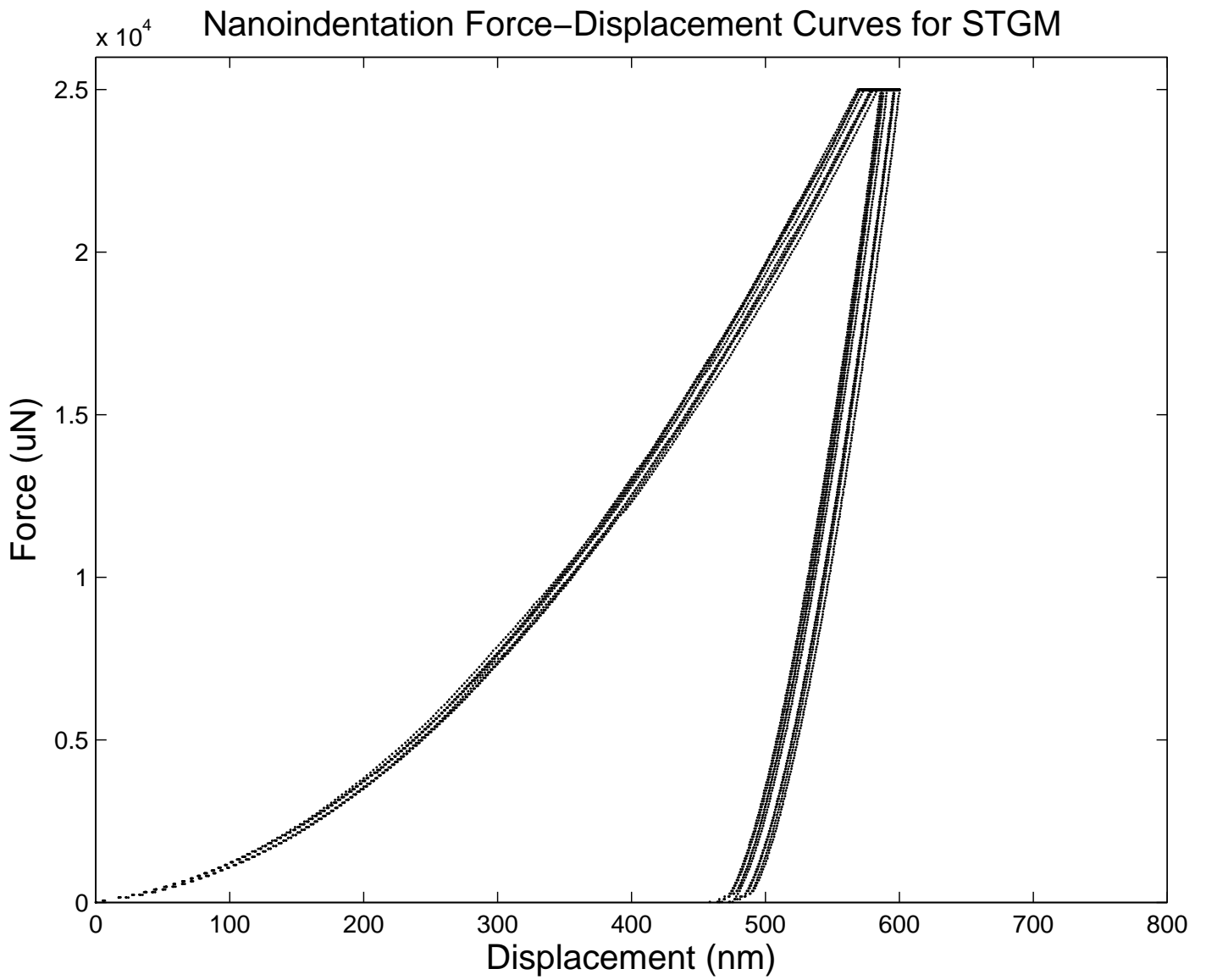
32 Table 1: Results from conventional “g•b” analysis of the main observed dislocation groups.  
33  
34

35 Table 2: Experimental parameters and results from previous indentation investigations, along  
36 with the present study, are summarized. Observation of counter-rotational lobes adjacent to the  
37 indent is consistent between all studies. The present study is distinguished from prior studies in  
38 utilizing the NPD technique with small (1.2nm) step size to investigate a BCC material.  
39  
40  
41  
42  
43  
44  
45  
46  
47  
48  
49  
50  
51  
52  
53  
54  
55  
56  
57  
58  
59  
60  
61  
62  
63  
64  
65

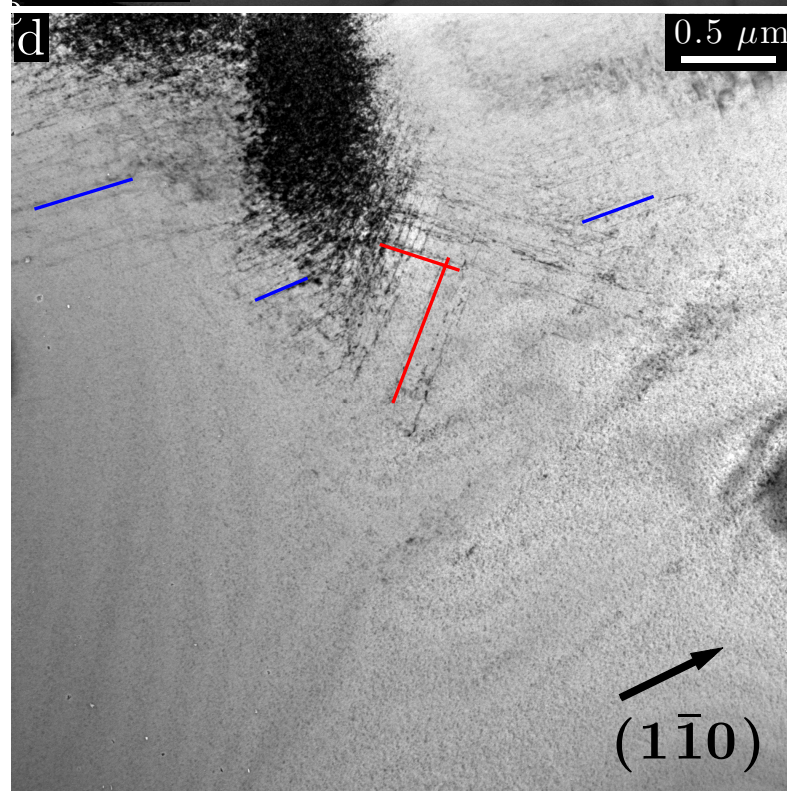
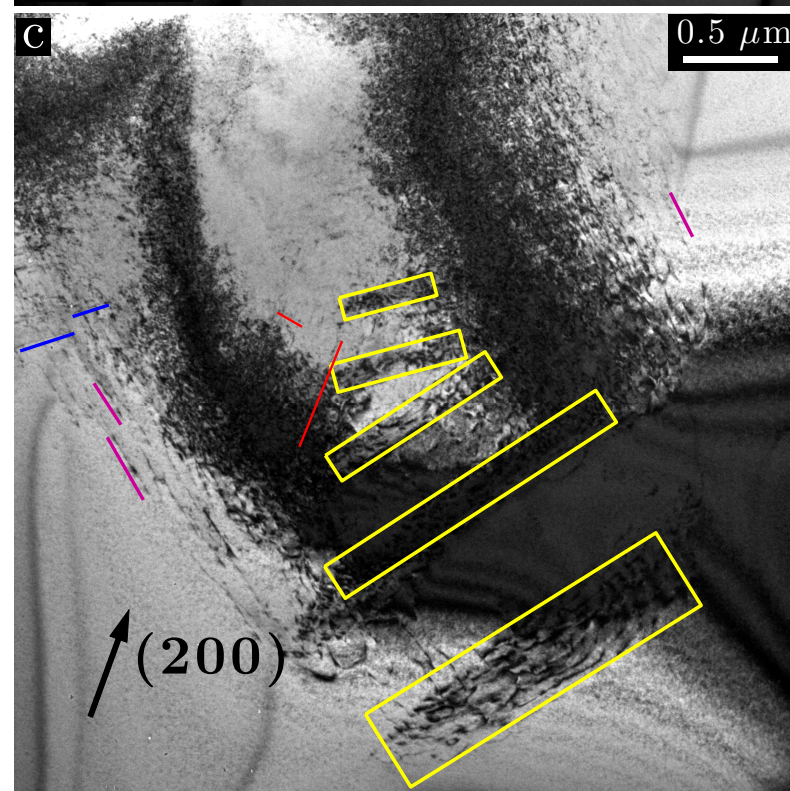
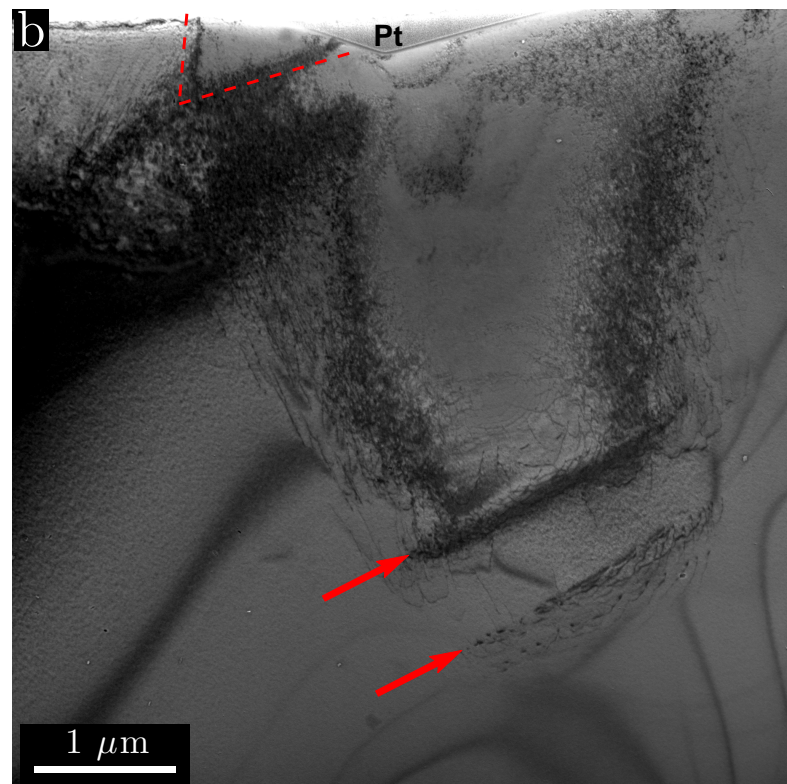
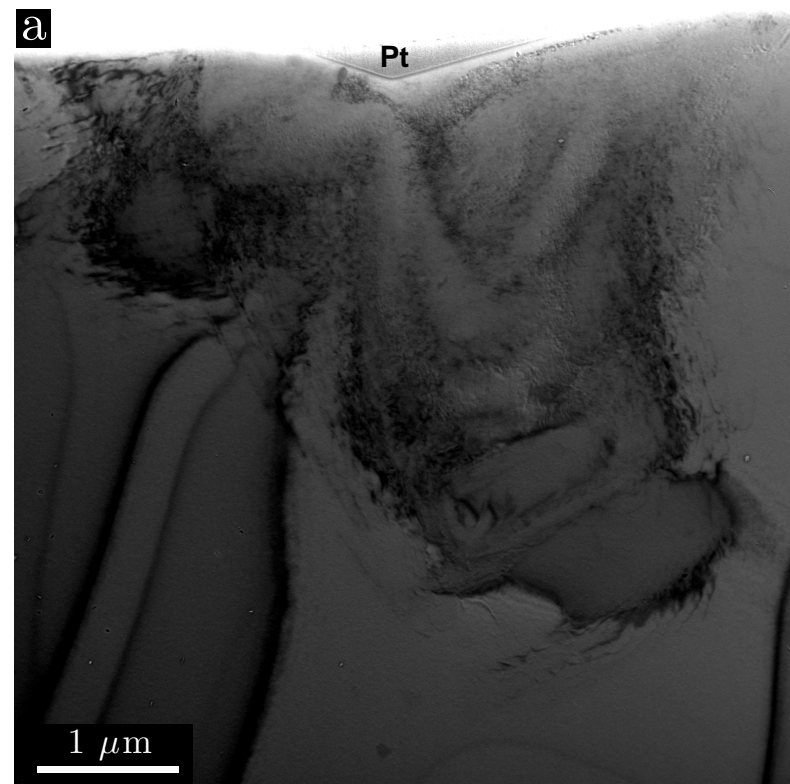
\*Figure(s) 1

▼ Diamond Berkovich Indenter

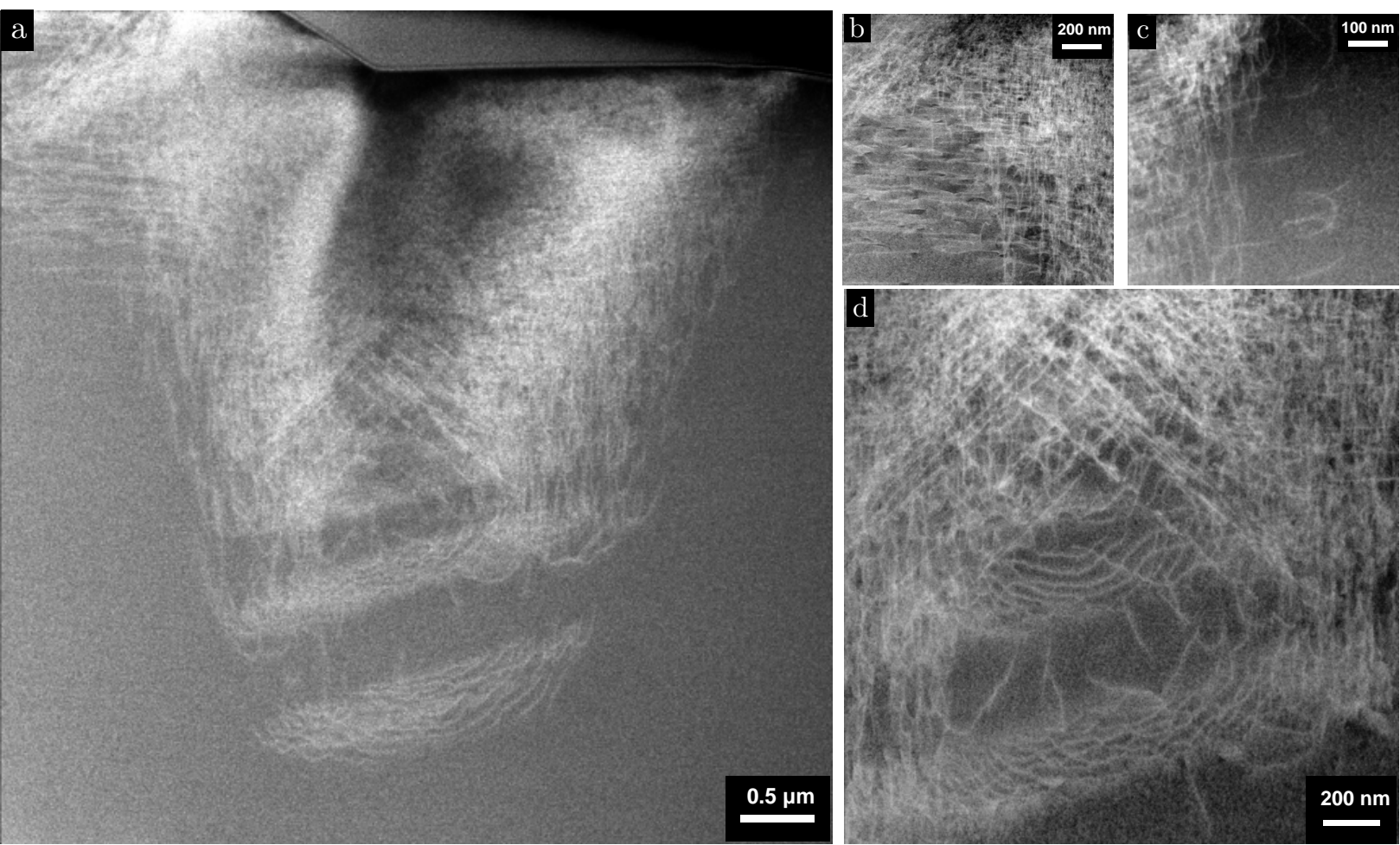




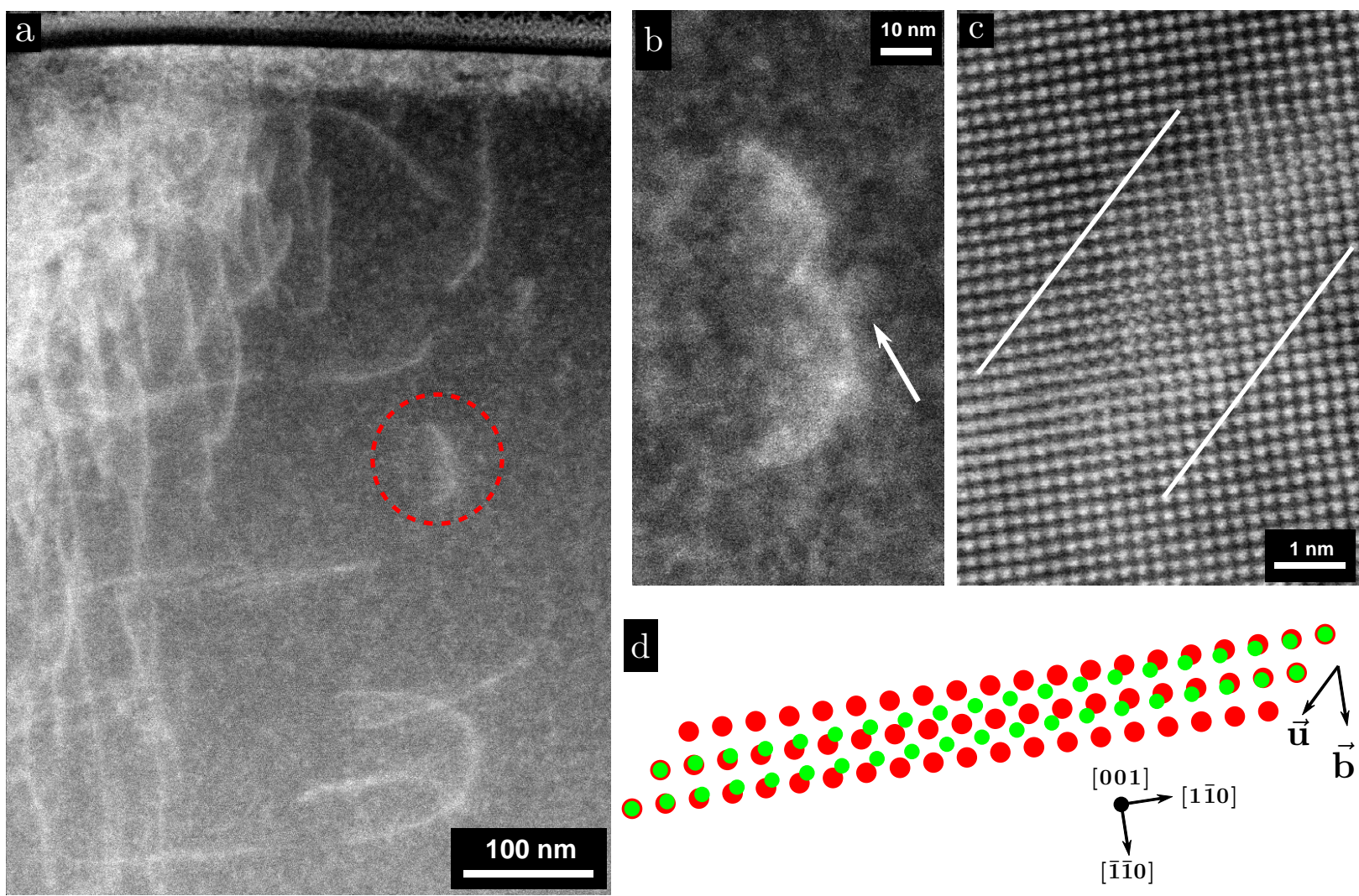
\*Figure(s) 3



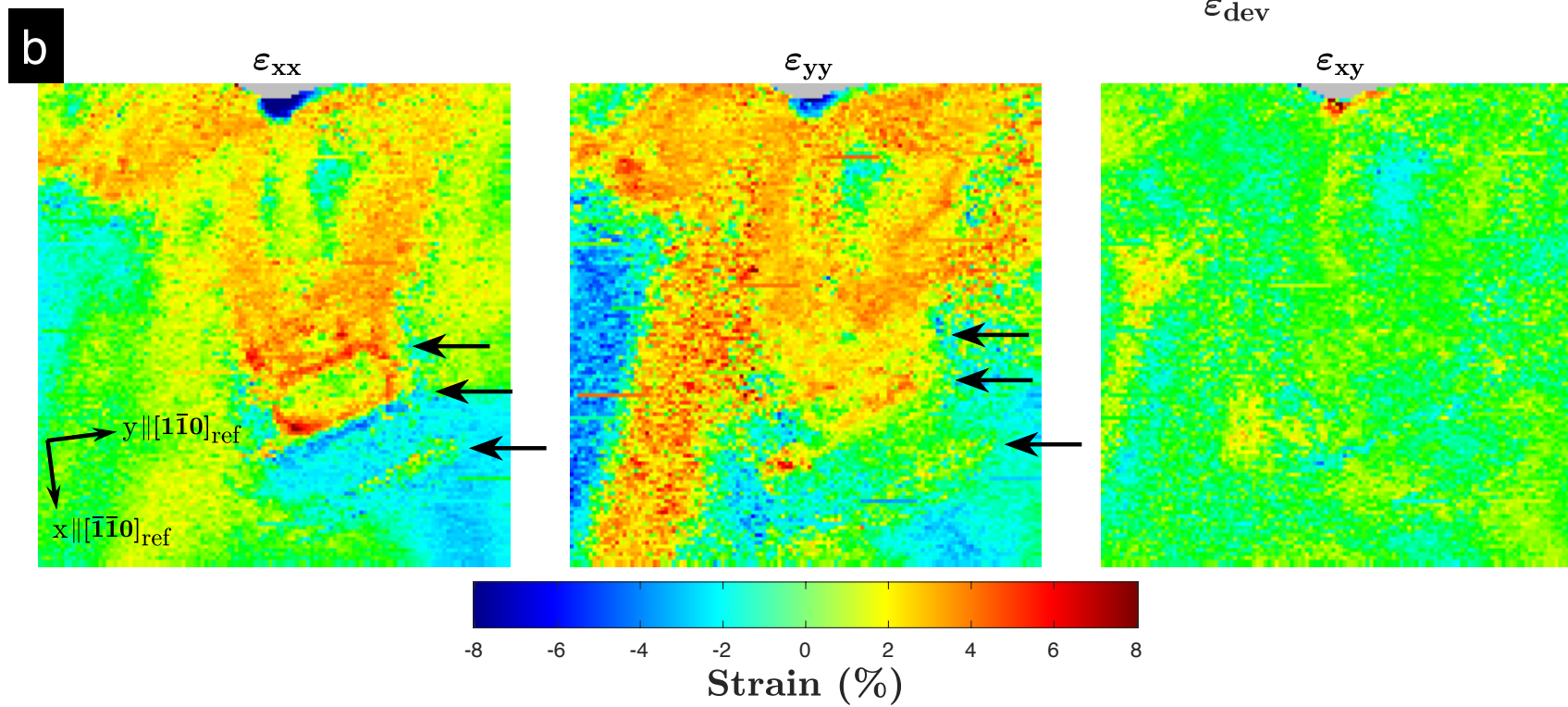
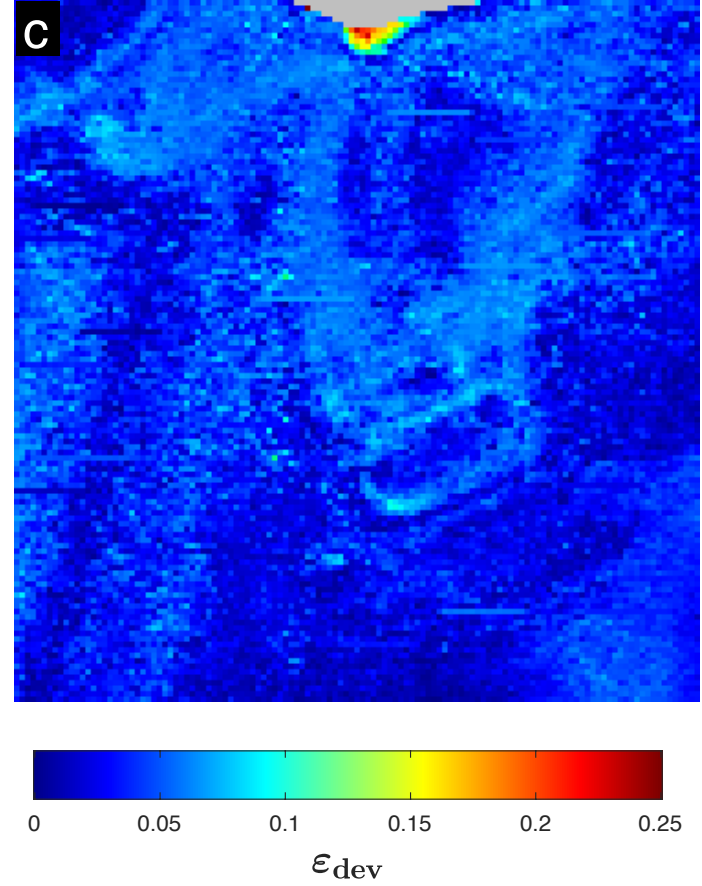
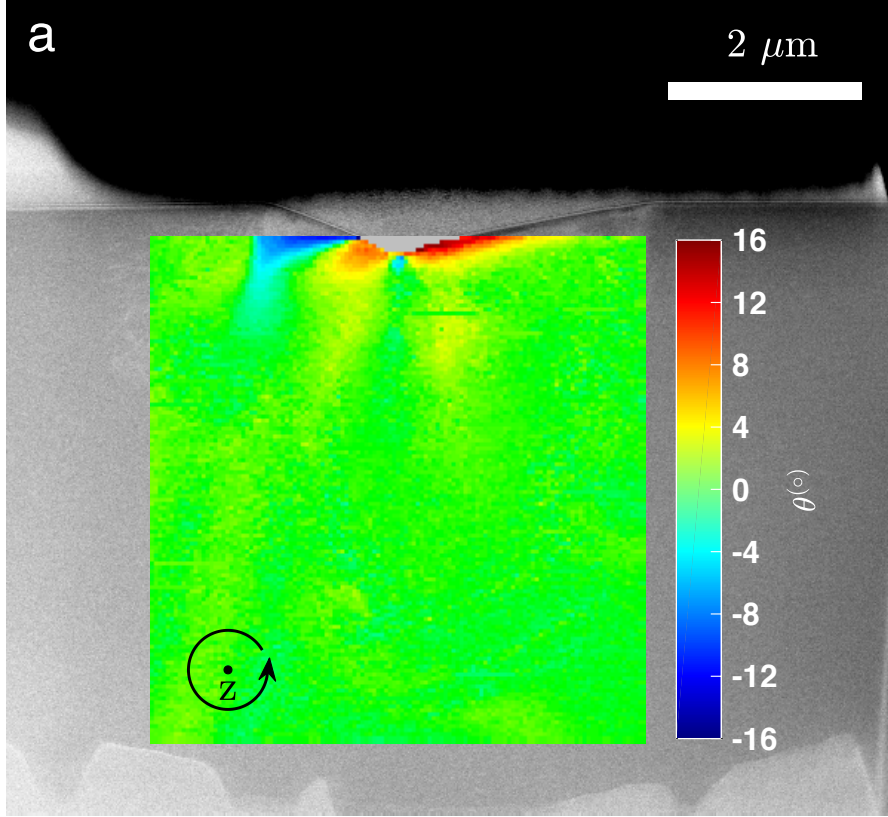
\*Figure(s) 4



\*Figure(s) 5

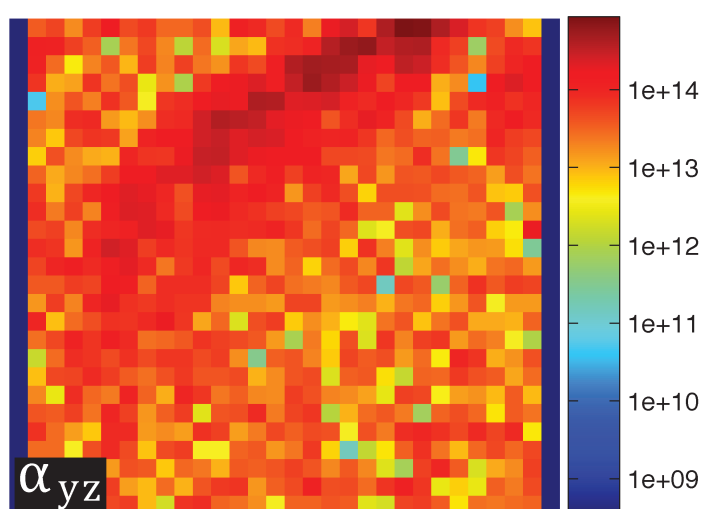
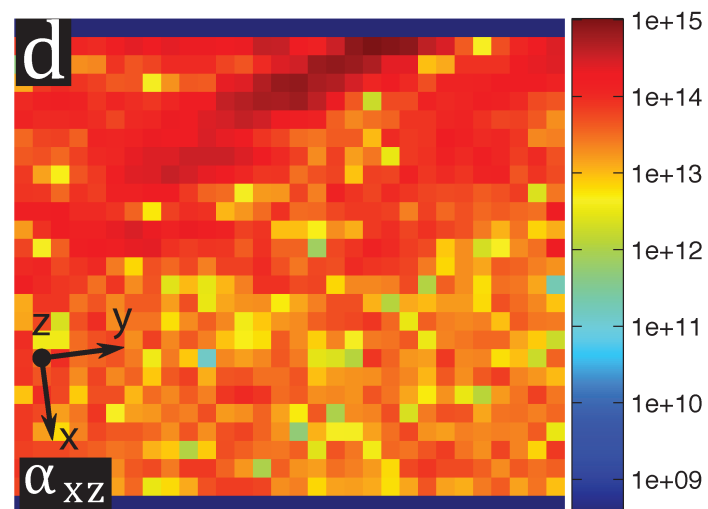
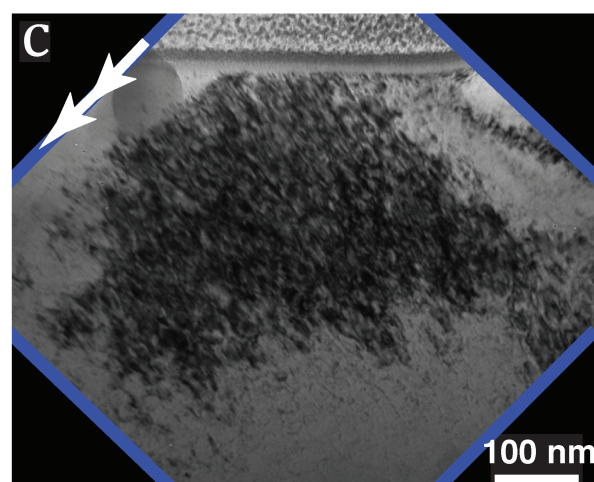
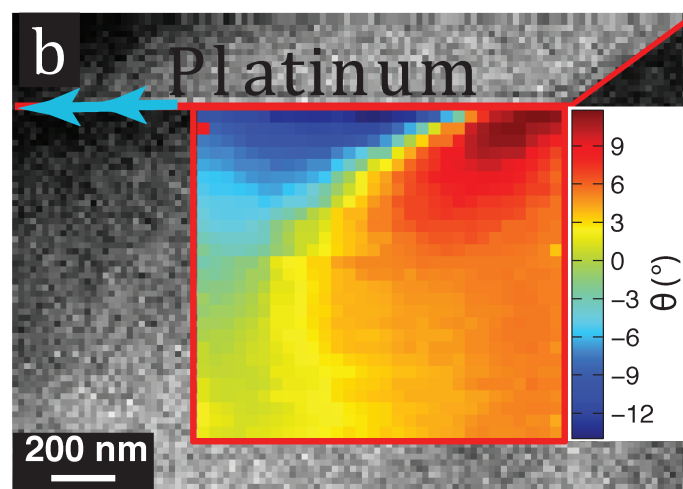
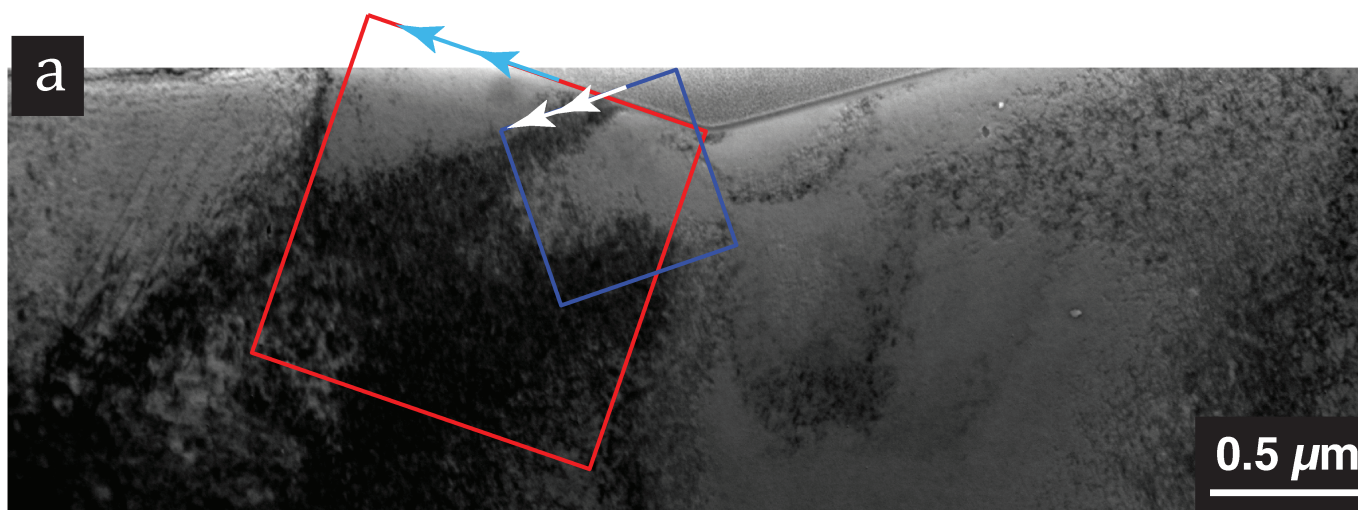


Figure(s) 6

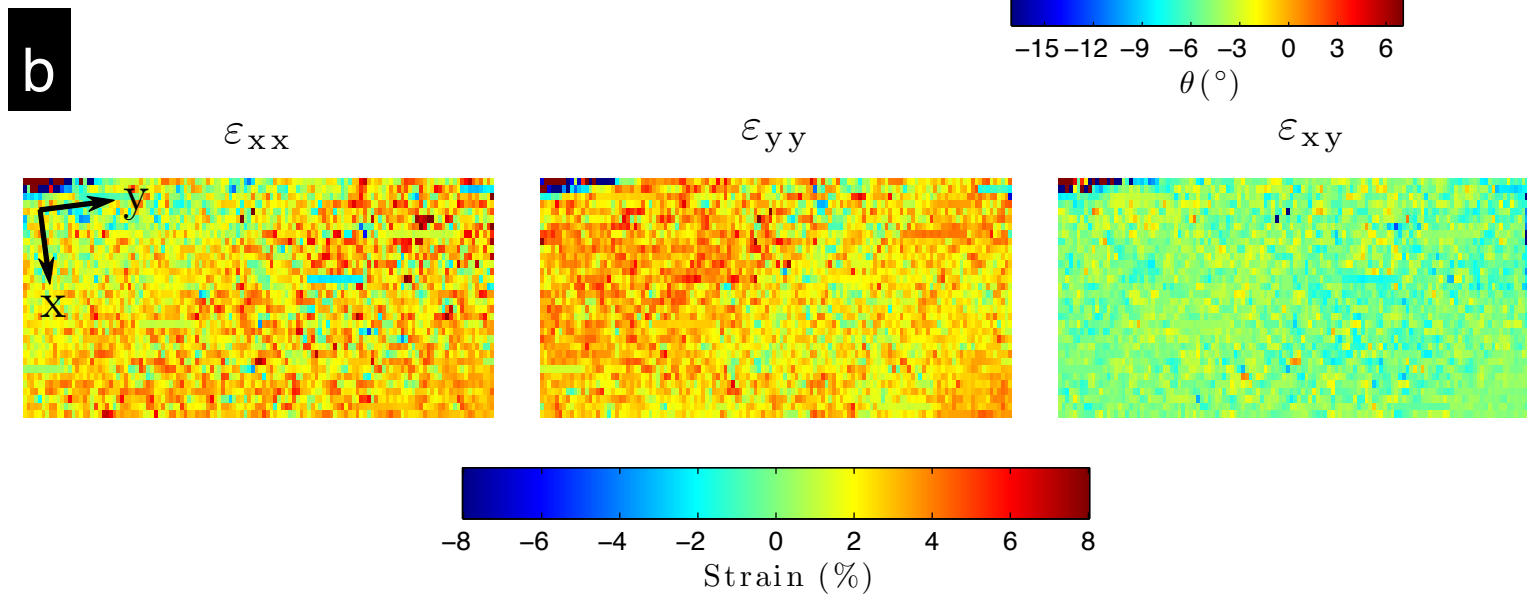
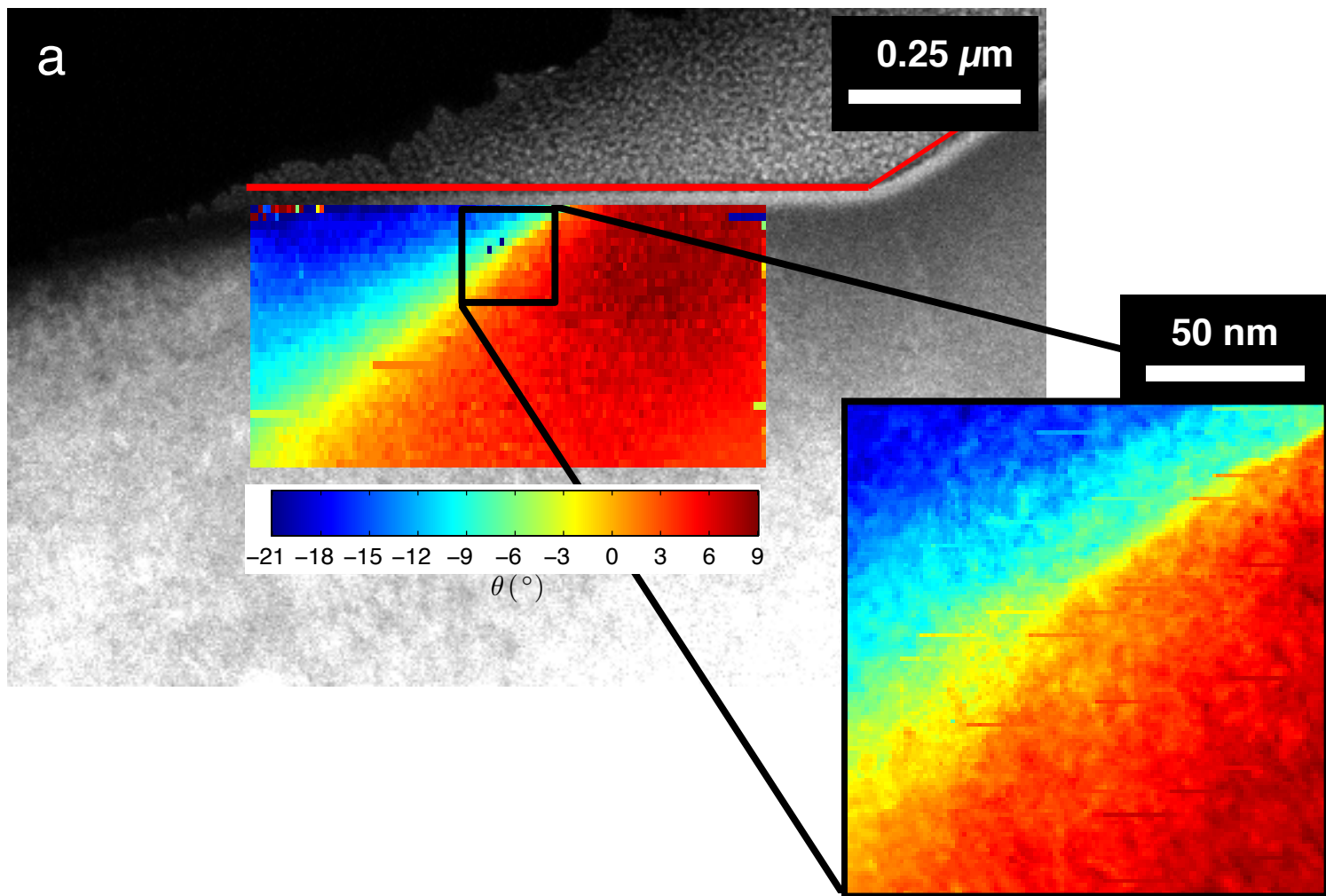




\*Figure(s) 7



\*Figure(s) 8



Table(s) 1

Dislocation group	G=200	G= 1-10	G=21-1	G=1-21	G=12-1	Burgers vector, <b>b</b>	Sense vector, <b>u</b>	Slip System
H	Visible	Visible	--	Visible	Unclear	$a/2 [1-11]$ or $a/2[-111]$	[1-11]	Screw or [-111](110)
V	Visible	Invisible	Visible	Visible	--	$a/2[-1-11]$	[-1-11]	Screw
SU	Visible	Visible	--	Visible	--	$a/2 [1-11]$ or $a/2[-111]$	[200]	[1-11](0-11) or [-111](011)
SD	Visible	Visible	--	Visible	--	$a/2 [1-11]$ or $a/2[-111]$	[0-20]	[1-11](011) or [-111](101)
	G=200	G=1-10	G=110	G=-21-1	G=1-2-1			
SB	Visible	Invisible	Visible	Visible	Invisible	$a/2[111]$	Straight segments [1-10]	[111](-1-12)

Table(s) 2

Study	Material	Technique(s)	Indentation Parameters	Observations	Proposed Mechanism
Lloyd et al. (2005)	Cu (FCC)	TEM – SAD (~0.5um step size) TEM imaging	Nanoindentation Load: 5mN Indentation direction: <001>	-Lattice rotations adjacent to indent	Martensitic shuffling: calculated effective GND up to $2.5 \times 10^{15}/m^2$
Kysar et al. (2007)	Cu, Al (FCC, single crystal)	EBSD: 3-5um step size	Indentation – Wedge Depth: 400, 750nm Indentation direction: [00-1] with wedge parallel to [110]	-Lattice rotation discontinuities adjacent to indent (counter rotational lobes present, separated by rotation free areas)	Dislocation slip: Calculated GND up to $\sim 8 \times 10^{14}/m^2$
Zaafarani et al. (2007)	Cu (FCC)	EBSD: 80nm step size	Nanoindentation - Conical Depth: up to 1um Indentation direction: <111>	- Six counter rotational lobes adjacent to indent separated by rotation free areas	Dislocation slip: counter rotational lobes due to changing loading axis activating different slip systems
Rester et al. (2007)	Cu (FCC, single crystal)	EBSD: 20nm step size TEM imaging of dislocation arrangement	Nanoindentation - Berkovich Load: 2.5-10mN Depth: 300nm Indentation direction: <111>	-Counter rotational “zones” adjacent to indent, no obvious rotational free zones -Subgrain formation beneath indenter tip	Dislocation slip: lobes produced by dislocation pile-up forming small angle grain boundary structures
Present study (2017)	Solution Treated Gum Metal (BCC, 50-100um grain size)	TEM - NPD: 40nm, 13.4x7.6nm, 1.2nm step sizes TEM/STEM imaging of dislocation arrangement, g.b analysis	Nanoindentation - Berkovich Load: 25mN Depth: 500nm Indentation direction: <110>	-Four counter rotational lobes adjacent to indent, continuous rotation, no presence of rotation free areas -Dislocation arrangement -Shear bands -Small angle grain boundaries	Dislocation slip: Continuous lattice rotations accommodated by large GND up to $\sim 10^{15}/m^2$

**Supplementary Material**

[Click here to download Supplementary Material: RPSankaran\\_Supplementary Materials\\_Acta Mater.docx](#)

**Supplementary Material Figure 1**

[Click here to download Supplementary Material: Supplementary\\_Figure\\_01.pdf](#)

**Supplementary Material Figure 2**

[Click here to download Supplementary Material: Supplementary\\_Figure\\_02.pdf](#)

**Supplementary Material Figure 3**

[Click here to download Supplementary Material: Supplementary\\_Figure\\_03.pdf](#)



**Supplementary Material Figure 4**

[Click here to download Supplementary Material: Supplementary\\_Figure\\_04.pdf](#)

